

Mathematical Modeling of Inertial Measurement Units

FINAL REPORT

Submitted to:

**Dr. Jason C. Chuang
EV42
Guidance, Navigation and Mission Analysis Branch
NASA Marshall Space Flight Center
MSFC, AL**

Submitted by:

**David A. Cicci, Ph.D., P.E.
Faculty Associate
Dynamic Concepts, Inc.**

August 21, 2006

Table of Contents

	<u>Page</u>
1.0 Introduction	1
2.0 Objectives	4
3.0 Background	4
4.0 Accelerometers	7
4.1 Translational Proof-Mass Accelerometer	8
4.2 Pendulous/Torque-Balance Accelerometer	15
5.0 Gyros	19
5.1 Spring-Restrained Rate Gyro	21
5.2 Rate Integrating Gyro	27
5.3 Ring Laser Gyro	33
5.4 Interferometric Fiber Optic Gyro	38
5.5 Coriolis Vibratory Gyro	43
5.6 Dynamically Tuned Gyro	48
6.0 Allan Variance Techniques	56
7.0 Summary and Conclusions	57
8.0 Recommendations for Future Development	58
9.0 Contact Information	59
10.0 References	60
11.0 SIMULINK Block Diagrams	64

List of Figures

	<u>Page</u>
Figure 1. System Model	3
Figure 2. Translational Proof-Mass Accelerometer Open-Loop Block Diagram (Dynamics-Only)	10
Figure 3. Translational Proof-Mass Accelerometer Closed-Loop Block Diagram (Dynamics-Only)	10
Figure 4. Translational Proof-Mass Accelerometer Closed-Loop Block Diagram	14
Figure 5. Pendulous/Torque-Balance Accelerometer Open-Loop Block Diagram (Dynamics-Only)	16
Figure 6. Pendulous/Torque-Balance Accelerometer Closed-Loop Block Diagram (Dynamics-Only)	16
Figure 7. Pendulous/Torque-Balance Accelerometer Closed-Loop Block Diagram	18
Figure 8. Spring-Restrained Rate Gyro	21
Figure 9. Spring-Restrained Rate Gyro Open-Loop Block Diagram (Dynamics-Only)	22
Figure 10. Spring-Restrained Rate Gyro Closed-Loop Block Diagram (Dynamics-Only)	23
Figure 11. Spring-Restrained Rate Gyro Closed-Loop Block Diagram	26
Figure 12. Rate-Integrating Gyro Open-Loop Block Diagram (Dynamics-Only)	28
Figure 13. Rate-Integrating Gyro Closed-Loop Block Diagram (Dynamics-Only)	29
Figure 14. Rate-Integrating Gyro Closed-Loop Block Diagram	32
Figure 15. Ring Laser Gyro Open-Loop Block Diagram (No Errors)	34
Figure 16. Ring Laser Gyro Coordinate System and Misalignment Angles	34
Figure 17. Ring Laser Gyro Closed-Loop Block Diagram	37
Figure 18. Interferometric Fiber Optic Gyro Open-Loop Block Diagram (No Errors)	39

List of Figures (cont.)

	<u>Page</u>
Figure 19. Interferometric Fiber Optic Gyro Coordinate System and Misalignment Angles	39
Figure 20. Interferometric Fiber Optic Gyro Closed-Loop Block Diagram	42
Figure 21. Coriolis Vibratory Gyro Coordinate System and Misalignment Angles	43
Figure 22. Coriolis Vibratory Gyro Closed-Loop Block Diagram	47
Figure 23. Dynamically Tuned Gyro Mechanical Schematic and Misalignment Angles	49
Figure 24. Dynamically Tuned Gyro Closed-Loop Block Diagram (Dynamics-Only)	51
Figure 25. Dynamically Tuned Gyro Closed-Loop Block Diagram	55

Mathematical Modeling of Inertial Measurement Units

David A. Cicci, Ph.D., P.E.
Faculty Associate
Dynamic Concepts, Inc.

1.0 Introduction

I was employed by Dynamic Concepts, Inc. (DCI) as a Faculty Associate for a total of 500 hours during the period between April 21, 2006 and September 29, 2006, to assist on the inertial measurement unit (IMU) modeling effort, which was included under the Task Order Title of Advanced Navigation Analysis and Design.

Most of the labor hours were performed during my temporary (summer) leave from Auburn University, where I hold the position of Professor of Aerospace Engineering. A small number of the total hours were performed at Auburn University during the period of time after August 4, 2006. My Faculty Associate Services Agreement with Dynamic Concepts, Inc. was arranged by DCI personnel Dr. Tom Howsman, President, Ms. Susan Howsman, Contract Administrator, and Mr. Phil Williams, Technical Program Manager, who also served as my Technical Point of Contact. Funding for this project was made available from NASA through subcontract with Jacobs Sverdrup under Customer Task Order #32-040202-00. My work location in Huntsville was Building 4600 at the George C. Marshall Space Flight Center. The Technical Program Manager at NASA who directed this IMU Modeling effort was Dr. Jason C. H. Chuang.

The Scope of the Statement of Work under the Task Order of Advanced Navigation Analysis and Design was defined to be associated with Crew Launch Vehicle (CLV) navigation system requirements development, analysis, equation derivation, algorithms development and implementation, architecture, design, implementation, evaluation, and possible testing.

This Statement of Work included a general description of four tasks to be addressed under this contractual agreement: Task 1 required developing navigation process equations, error equations, and mathematical models used for navigation performance analysis and navigation system simulation; Task 2 required developing and implementing algorithms used for navigation performance analysis and navigation system simulation; Task 3 required designing and evaluating navigation system architectures; and, Task 4 required meeting and interacting with guidance and control engineers as well as other subsystem groups to furnish and request needed information and data.

The Milestones and Deliverables required under this Statement of Work were defined as: i) monthly activity reports (MARS) describing the technical progress and findings; ii) mathematical equations, models, and algorithms if requested and developed

for the tasks; iii) and, software source codes if requested and developed for the tasks. In addition, periodic meetings were held with Jason Chuang to discuss the project specifics, and IMU Status Reports were provided to both Jason Chuang and Phil Williams on a regular basis.

The specific focus of this project was directed towards the development of a generalized, high fidelity mathematical model of an IMU to be used as a future analysis tool capable of simulating the performance of commercially available units. The original intent was to develop a mathematical model that would possess the capability to use data from manufacturer's product specifications to be able to closely mimic the performance of manufacturer's units. However, Ang, et al (2004), indicate that it is unlikely that accurate simulations of commercial units can be achieved solely with the information provided to the customer in the product specifications. In most cases it would appear that significant testing of a unit is necessary in order to determine a substantial set of error modeling parameters to be used in modeling the units. Without adequate testing it is unlikely that a highly accurate model of an IMU or its components can be developed.

In the development of this type of model, it was extremely important to completely address the modeling of the many possible error sources which may occur during the IMU measurement process. These error sources can consist of a variety of perturbation, environmental, and stochastic errors. Although product specification sheets generally do not provide information on all types of errors which affect the performance of the IMU, some common error sources which are often provided include bias, scale factor, and misalignment.

Also important in the development of a high fidelity IMU mathematical model is the capability to combine the error model with the physical/dynamical model and the stochastic model of the unit. This approach will provide the ability to predict system response and time delays more accurately to better represent real-world performance. A system model of a general sensor which combines the physical model and stochastic model with the various models of the error sources is suggested in by the Institute of Electrical and Electronics Engineers (IEEE) (1999) and is shown in Figure 1 below.

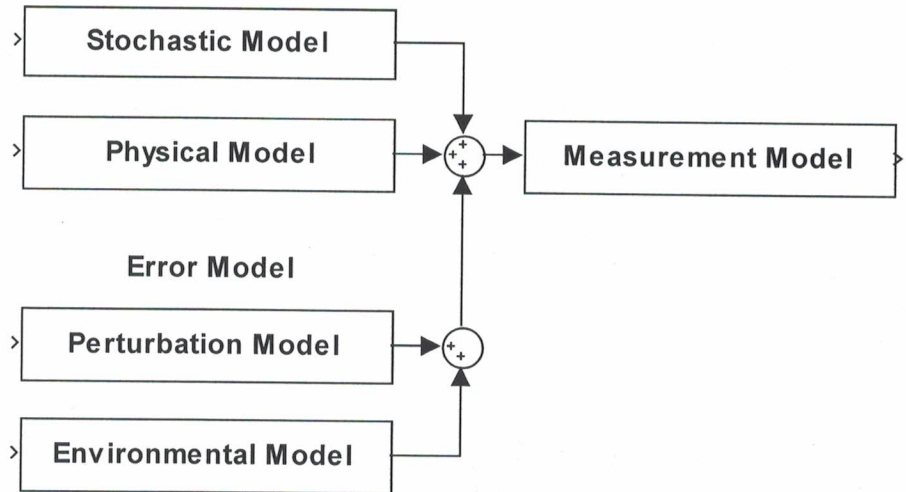


Figure 1. System Model

The dynamical/physical models are described by algebraic or differential equations that represent the physics of the system's operation. This portion of the model is deterministic and can generally be addressed with dynamical modeling techniques. The perturbation model consists of sensitivities to variations in the parameters in the physical equations, while the environmental model consists of sensitivities to environmental disturbances. The stochastic model includes any random drift-type errors that generally occur during normal operation of the unit. The measurement model is also shown in Figure 1 and relates the physical states of the system to the measurements being made, along with a component of random measurement noise.

One approach to combining the dynamical/physical and error models for any unit or device is through the development of a block diagram model and the corresponding transfer function relating the output to the input for specific IMU or its components. That approach is taken in this study in order to best combine the individual models into a single, high fidelity model. This block diagram/transfer function approach is well suited for the subsequent development of a software simulation using commercially available programs such as SIMULINK, PSPICE, or a similar analysis tool. Once block diagrams are generated, they can be converted to a functioning simulation without a substantial program of effort.

After an extensive review of the literature, it was determined that the best procedure to developing a generalized, high fidelity, mathematical model of an IMU was to model the individual sensors, i.e., the accelerometers and gyros, separately. This methodology allows for more flexibility in modeling errors in each component and ultimately provides for improved accuracy in the IMU performance. It also provides a better framework for changing or modifying particular components within an IMU for

possible future design, analysis, and feasibility studies. Under this approach, a number of the most common types of accelerometers and gyros were addressed in this study. These components include: translational proof-mass and pendulous/torque-balance accelerometers and, spring-restrained rate, rate-integrating, ring laser, interferometric fiber optic, Coriolis vibratory, and dynamically tuned gyros.

The sections below discuss the project objectives, and background of the problem being addressed, and provide detailed descriptions of the mathematical models which have been developed for each type of accelerometer and gyro which was studied. Finally, conclusions and a set of recommendations for further development are presented. A complete list of the references cited in this document is also provided in bibliographical form.

2.0 Objectives

Considering the approach discussed above, several primary objectives were established for this IMU modeling project. These objectives are stated as:

1. Perform a literature review to determine the current state-of-the-art methods for developing mathematical models for accelerometers and gyro.
2. Develop the dynamical/physical models for the common types of accelerometers and gyros.
3. Develop high fidelity error models for the common types of accelerometers and gyros.
4. Create appropriate block diagrams which combine the dynamical/physical models with the error models for the various sensors models being developed.
5. Determine mathematical expressions for the sensor output in terms of the sensor input for each sensor model.

The literature review will be presented in the Background section, while the other objectives will be addressed in separate sections for each type of sensor studied.

3.0 Background

For most aerospace applications, IMUs typically consist of orthogonally-mounted clusters of three accelerometers and three gyros in order to provide the IMU with the capability to detect six degree-of-freedom motion in a vehicle by providing three components of acceleration and rotation rate outputs. These accelerometers and gyros detect and measure motion based on the physical laws of nature rather than on the detection of external signals (Farrell and Barth, 1999). The sensor outputs are provided to a computer-implemented numerical integration process which computes a navigation solution that yields a complete set of navigation state data, i.e., position, velocity, and attitude. This collection of sensors, computer, and navigation aids collectively referred to as an Inertial Navigation System (INS) (Rogers, 2003).

Many different types of accelerometers and gyros exist today and others are currently being developed. Sensors were originally developed as mechanical and electro-mechanical devices but have since gone through several variations to take advantage of the latest available technology.

Barbour and Schmidt (2001) provide a discussion of current trends in inertial sensor technology, along with graphical representations of applications and showing relative scale-factor and bias stability comparisons. It is also stated that “ongoing trends in inertial sensor technology development are focused on interferometric fiber-optic gyros, micro-mechanical gyros and accelerometers, and micro-optical sensors. Micromechanical sensors and improved fiber-optic gyros are expected to replace many of the current systems which use ring laser gyros or mechanical sensors. The introduction of the new technologies is primarily driven by cost and cost projections for systems using these technologies. Externally aiding the INS with the global positioning system (GPS) has opened up the ability to navigate a wide variety of new, large-volume applications, which are driving the need for extremely low-cost, batch-producible sensors.”

During the process of detecting motion, measurement errors are generated by all sensors. These errors contribute to the total errors in the position, velocity, and attitude of the vehicle computed by the INS and can result in unbounded growth over time due to the integration of inertial measurements during INS implementation. It is therefore, critical to develop accurate error models for the sensors.

Many references are available which address the mathematical modeling of INS errors resulting from combined accelerometer and gyro errors, including: Maybeck (1979), Kim, et al (1996), Farrell and Barth (1999), Grewel, Weill, and Andrews (2001), Park and Tan (2002), and Rogers (2003). In addition, the general literature includes references which address errors in specific types of accelerometers and gyros, including: Craig (1972a, 1972b, 1990), Chung, et al (2001a, 2001b), Ang (2004), Park (2004), and Dorobantu and Gerlach (2004). Brown (2005) describes the use of an integrated GPS/INS system that uses commercial off-the-shelf accelerometers and gyros.

The references cited in the previous paragraph only consider a few of the possible error sources, however. Common error sources which are modeled in these studies include bias, scale factor, input axis misalignment, and random measurement noise. Occasionally, errors due to nonlinearity, g sensitivity, time correlated effects, and random walk errors are also included. There are a number of other error sources which also contribute significantly to the errors contained in the output of accelerometers and gyros. Few references in the general literature present comprehensive error models for the types of sensors being considered in this study. One which does is Junqueira and de Barros (2004). This type of comprehensive modeling of the many error sources in both accelerometers and gyros must be performed in order to significantly enhance the capability to accurately model the performance of IMUs.

During this project it was found that the most useful references were a series of specifications, standards, and testing procedures published by the Institute of Electrical

and Electronics Engineers (IEEE). The inertial sensors standards were developed by the Gyro and Accelerometer Panel of the IEEE Aerospace and Electronics Systems Society, and are published by the Standards Association of the IEEE. The Gyro and Accelerometer Panel has been meeting bi-monthly for nearly 40 years in order to develop a comprehensive set of standards for accelerometers and gyros. More information about the IEEE Gyro and Accelerometer Panel can be found on the following Web site: <http://grouper.ieee.org/groups/gap>.

Sensor standards which have been published include those for single and two-degree of freedom spinning wheel gyros, laser gyros, interferometric fiber optic gyros, angular accelerometers, linear accelerometers, accelerometer centrifuge testing, and inertial sensor terminology documents. A discussion of these standards is provided by Thielman, et al (2002) and Curey, et al (2004). The published IEEE standards which are pertinent to this study are listed below.

IEEE Std. 292-1969 (R2000):	IEEE Specification Format for Single-Degree-of-Freedom Spring-Restrained Rate Gyros
IEEE Std. 293-1969 (R2000):	IEEE Test Procedure for Single-Degree-of-Freedom Spring-restrained Gyros
IEEE Std. 517-1974 (R2000):	IEEE Standard Specification Format Guide and Test Procedure for Single-Degree-of-Freedom Rate-Integrating Gyros
IEEE Std. 529-1980 (R2000):	IEEE Supplement for Strapdown Applications to IEEE Standard Specification Format Guided and Test Procedure for Single-Degree-of-Freedom Rate-Integrating Gyros
IEEE Std. 530-1978 (R1986):	IEEE Standard Specification Format Guide and Test Procedure for Linear, Single-Axis, Digital, Torque-Balance Accelerometer
IEEE Std. 647-1995:	IEEE Standard Specification Format Guide and Test Procedure for Single-Axis Laser Gyros
IEEE Std. 813-1988 (R2000):	IEEE Specification Format Guide and Test Procedure for Two-Degree-of-Freedom Dynamically Tuned Gyros
IEEE Std. 836-2001:	IEEE Recommended Practice for Precision Centrifuge Testing of Linear Accelerometers

IEEE Std. 952-1997 (R2003):	IEEE Standard Specification Format Guide and Test Procedure for Single-Axis Interferometric Fiber Optic Gyros
IEEE Std. 1293-1998 (R2003):	IEEE Standard Specification Format Guide and Test Procedures for Linear, Single-Axis, Non-Gyroscopic Accelerometers
IEEE Std. 1431-2004:	IEEE Standard Specification Format Guide and Test Procedure for Coriolis Vibratory Gyros

While their use is voluntary, the standards developed by the IEEE represent a consensus of the broad expertise on the subject within the IEEE as well as those outside the IEEE that have expressed an interest in participating in the development of the standards. The standards are provided as a guide for the preparation of a specification and a test procedure for the specific accelerometer or gyro of interest.

Based on the information available from the literature search and that contained in the IEEE standards, it has been determined that this study will focus on the development of mathematical models for translational proof-mass and pendulous/torque-balance accelerometers, and spring-restrained rate, rate-integrating, ring laser, interferometric fiber optic, Coriolis vibratory, and dynamically tuned gyros. The sections below will present a general discussion of accelerometers and gyros, along with specific discussions and the mathematical models which have been developed for each particular type of sensor studied.

4.0 Accelerometers

Thielman (2002) and Curey, et al (2004) provide general descriptions of linear accelerometers and the applicable standards. Portions of those discussions are reproduced in this section.

A linear accelerometer is an inertial sensor that measures the component of translational acceleration minus the component of gravitational acceleration along its input axes. An output signal is produced from the motion of a proof-mass relative to the case, or from the force or torque required to restore the proof-mass to a null position relative to the case. Piezoelectric accelerometers, used to measure accelerations by the strain on a piezoelectric sensor attached to a proof-mass, such as during vibration tests, are not discussed, nor are gyroscopic accelerometers or gravimeters that have a narrow range of applications.

The pickoff for proof-mass movement in a macro-sized force-rebalance accelerometer could be electromagnetic, capacitive, or optical. The force or torquer required to restore the proof-mass to the null position is usually electromagnetic.

However, the restoring force for a three-axis, low-g accelerometer for space applications is generally capacitive in nature.

A Vibrating Beam Accelerometer (VBA) has piezo-electrically driven quartz resonators or electrostatically driven silicon resonators attached to separate proof-masses or to a common proof-mass, where the measure of acceleration is the difference frequency of anti-parallel resonators for common mode rejection of many error effects.

Micro-Electro-Mechanical-Systems (MEMS) accelerometers are made from silicon or quartz chips using photolithographic and chemical etching techniques from the integrated circuit industry. The MEMS pendulous/torque-balance and translational proof-mass MEMS accelerometers are relatively low in cost. They are often open-loop devices, where the deflection of the proof-mass against an elastic restraint measured capacitively, piezo-resistively, or otherwise is the measure of acceleration. A MEMS accelerometer could be a force-rebalance design using a capacitive torquer or force. IEEE (2001) describes calibration of accelerometer higher order acceleration-sensitive model terms using a precision centrifuge.

IEEE (1999) provides a guide for specifying linear single-axis accelerometer performance and descriptions of tests for verifying this performance, both for general accelerometer characteristics and for specific types of accelerometers. Informative annexes describe specific types of nongyroscopic accelerometers, namely pendulous force-rebalance accelerometers, VBAs, and micromechanical accelerometers.

Mathematical models for both translational proof-mass and pendulous/torque-balance type accelerometers are presented in the section below. These mathematical models combine dynamical/physical models and high fidelity error models for each type of accelerometer into a system model represented by SIMULINK block diagrams. The error models contain a number of model parameters which represent different types of possible errors. The number of terms used in the model may be reduced depending on the amount and type of information about the errors, either from the manufacturer or from testing, that's available for implementation in the model.

Expressions for the output as functions of the input accelerations and model parameters are also provided for the system model for open and closed-loop representations. Models are presented for single-axis accelerometers which can be easily converted to a model for a three sensor cluster for implementation into a full IMU model.

4.1 Translational Proof-Mass Accelerometer

For a typical open-loop translational proof-mass accelerometer, the sensor responds to input acceleration $a(t)$ with a translational displacement of the proof-mass which is proportional to the acceleration. The dynamics of the translational proof-mass can be modeled as a standard spring-mass-damper system. The well-known equations of

motion of this type of system are presented by Farrell and Barth (1999), and many others as

$$m\ddot{x}(t) + C\dot{x}(t) + Kx(t) = F(t) \quad (1)$$

where:

- $x(t)$ = displacement of the proof-mass along the input axis, m
- $\dot{x}(t)$ = velocity of the proof-mass along the input axis, m/s
- $\ddot{x}(t)$ = sensed acceleration, $a(t)$, of the proof-mass along the input axis, m/s²
- m = proof-mass, g
- C = damping coefficient, g/s
- K = spring constant, N/m
- $F(t)$ = forcing function, N

Considering all initial conditions to be zero, the Laplace Transform of this equation can be taken to allow it to be written in the s-plane as

$$[ms^2 + Cs + K]x(s) = F(s) \quad (2)$$

where:

- s = Laplace operator
- $x(s)$ = Laplace Transform of the proof-mass displacement, $x(t)$, m
- $F(s)$ = Laplace Transform of the forcing function, $F(t)$, N

The transformed sensed acceleration, $a(s)$, is converted to the transformed forcing function, $F(s)$, using the relationship

$$F(s) = ma(s) \quad (3)$$

that is used to generate the output displacement, $x(s)$. The pickoff and electronics module sense the displacement of the proof-mass and convert it into a proportional electrical output signal, which can then be approximated by the following equation

$$V_o(s) = K_p K_a x(s) \quad (4)$$

where:

- $V_o(s)$ = Laplace Transfer of the output voltage, V_o
- K_p = pickoff transfer function, V/m
- K_a = output amplifier transfer function, V_{dc}/V_{ac}

Combination of Equations (2), (3) and (4) provide the expression for the accelerometer output, $V(s)$, in terms of the input, $a(s)$, as

$$V_o(s) = K_p K_a ma(s) / (ms^2 + Cs + K) \quad (5)$$

Equation (5) represents the standard dynamical open-loop transfer function for a translational proof-mass accelerometer and the corresponding block diagram is shown in Figure 2.

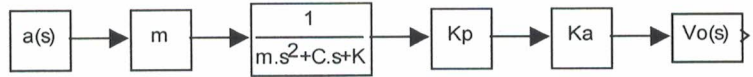


Figure 2. Translational Proof-Mass Accelerometer Open-Loop Block Diagram (Dynamics-Only)

As discussed by IEEE (1999), accelerometers can provide higher performance for critical applications by use of classical negative feedback, using a force acting on the translational proof-mass to minimize the displacement of the proof-mass when it is subjected to a force produced by acceleration of the sensor case. The open-loop model can be converted to a generalized closed-loop model by including a gain, K_f , in the feedback loop. The block diagram showing this feedback gain for the closed-loop dynamics of a translational proof-mass accelerometer is shown in Figure 3.

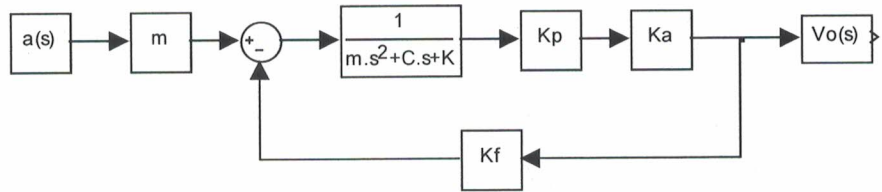


Figure 3. Translational Proof-Mass Accelerometer Closed-Loop Block Diagram (Dynamics-Only)

Using appropriate block diagram algebra, the accelerometer output for the closed-loop dynamics can be found as

$$V_o(s) = K_p K_a ma(s) / (ms^2 + Cs + K + K_f K_p K_a) \quad (6)$$

where K_f = feedback gain, N/V

IEEE (1999) also provides a model equation of an accelerometer which is defined as a series that mathematically relates the accelerometer output E to the components of the applied accelerations, angular velocities, and angular accelerations along the accelerometer reference axes. The reference axes are defined as IA in the longitudinal direction, PA in the lateral direction, and OA upward to form a right-handed system.

A simplified version of the model equation is presented by the IEEE (2001) which eliminates the sign-dependent and higher-order, dynamic-dependent terms. This will allow for improved determination of the modeling coefficients in the equation using data

obtained by testing of the unit. Following IEEE (2001), this modified model equation for the sensed acceleration can be written as

$$\begin{aligned} a(t) = E / K_1 &= a_i(t) + K_0 + C_1 a_i(t) + K_2 a_i(t)^2 + K_3 a_i(t)^3 \\ &+ \delta_o a_p(t) - \delta_p a_o(t) + K_{ip} a_i(t) a_p(t) + K_{io} a_i(t) a_o(t) \\ &+ K_{op} a_o(t) a_p(t) + K_{pp} a_p(t)^2 + K_{oo} a_o(t)^2 + \varepsilon(t) \end{aligned} \quad (7)$$

where

- $a(t)$ = sensed acceleration, g
- E = accelerometer output, V
- $a_i(t)$, $a_p(t)$, $a_o(t)$ = applied accelerations along the IA, PA, and OA axes, respectively, g
- K_0 = bias, g
- K_1 = scale factor, V/g
- C_1 = first-order coefficient, g/g
- K_2 = second-order coefficient, g/g²
- K_3 = third-order coefficient, g/g³
- δ_p , δ_o = misalignment of the IA axis with respect to the input reference axis about the OA and PA axes, respectively, rad
- K_{ip} , K_{io} , K_{op} = cross-coupling coefficients, g/g³
- K_{pp} , K_{oo} = cross-axis nonlinearity coefficients, g/g²
- $\varepsilon(t)$ = random measurement and process noise, g

The modeling coefficients in Equation (7) are K_0 , K_1 , C_1 , K_2 , K_3 , δ_p , δ_o , K_{ip} , K_{io} , K_{op} , K_{pp} , and K_{oo} . Of these modeling coefficients, the scale factor, K_1 , bias, K_0 , and axis misalignment coefficients, δ_p , and δ_o , can often be obtained from the manufacturer's specification sheets for commercially available accelerometers. The values of the other coefficients are generally not available from the manufacturer and must be obtained by testing and calibration of each unit. Additional information regarding the mathematical form, physical meaning, and procedures for accelerometer testing and calibration is provided by the IEEE (1978, 1999, and 2001). Upon performing the specified tests, the method of least squares can be used to determine the values of the model coefficients using the data obtained in the testing program.

The random measurement and process noise, $\varepsilon(t)$, could have quantization, white, random walk, flicker, or other components. The process noise distinct from the noise due to the analog-to-digital converter, voltage-to-frequency converter, or other digitization readout system can be regarded as accelerometer random bias instability, separate from any systematic models of bias variation such as trend or temperature and other sensitivities. Characterization of the measurement and process noise in the output observable can be performed using Allan variance techniques, which will be discussed later in this report. The process noise can best be modeled in a guidance system Kalman filter model using augmented Markov process states. As a result, the random process noise will not appear in the model equation upon taking the Laplace Transform of Equation (7).

Taking the Laplace Transform of Equation (7) gives an expression for the sensed acceleration for use in the corresponding block diagram becomes

$$\begin{aligned} a(s) &= E(s)/K_1 = a_i(s) + K_0 + C_1 a_i(s) + K_2 a_i(s)^2 + K_3 a_i(s)^3 \\ &\quad + \delta_o a_p(s) - \delta_p a_o(s) + K_{ip} a_i(s) a_p(s) + K_{io} a_i(s) a_o(s) \\ &\quad + K_{op} a_o(s) a_p(s) + K_{pp} a_p(s)^2 + K_{oo} a_o(s)^2 \end{aligned} \quad (8)$$

Equation (8) can be written as the sum of the applied acceleration in the IA direction, $a_i(s)$, and the error in the sensed acceleration due to the accelerometer performance, Δa , as

$$a(s) = a_i(s) + \Delta a(s) \quad (9)$$

where

$$\begin{aligned} \Delta a(s) &= K_0 + C_1 a_i(s) + K_2 a_i(s)^2 + K_3 a_i(s)^3 + \delta_o a_p(s) \\ &\quad - \delta_p a_o(s) + K_{ip} a_i(s) a_p(s) + K_{io} a_i(s) a_o(s) + K_{op} a_o(s) a_p(s) \\ &\quad + K_{pp} a_p(s)^2 + K_{oo} a_o(s)^2 \end{aligned} \quad (10)$$

This representation will allow direct integration of the error terms which will result in a more accurate model. A possible SIMULINK block diagram for the complete model combining the dynamical model and the error terms is shown in Figure 4. Intermediate outputs of velocity are shown for both the dynamic and error models.

Using appropriate block diagram algebra, the accelerometer output can be expressed in terms of the applied accelerations and the error terms as

$$\begin{aligned} V_o(s) &= mK_p K_a a_i(s) / (ms^2 + Cs + K + K_f K_p K_a) \\ &\quad + K_p K_a (ms^2 + Cs + K) \Delta a(s) / [(ms^2 + Cs + K + K_f K_p K_a) s^2] \end{aligned} \quad (11)$$

Substitution of Equation (10) into Equation (11) will give the expanded form of the accelerometer output as

$$\begin{aligned} V_o(s) &= \{mK_p K_a / (ms^2 + Cs + K + K_f K_p K_a) + K_p K_a (ms^2 + Cs + K) \\ &\quad (C_1 + K_{ip} a_p(s) + K_{io} a_o(s)) / [(ms^2 + Cs + K + K_f K_p K_a) s^2]\} a_i(s) \\ &\quad + \{K_p K_a (ms^2 + Cs + K) / [(ms^2 + Cs + K + K_f K_p K_a) s^2]\} \\ &\quad [K_2 a_i(s)^2 + K_3 a_i(s)^3 + K_0 + \delta_o a_p(s) - \delta_p a_o(s) + K_{op} a_o(s) a_p(s) \\ &\quad + K_{pp} a_p(s)^2 + K_{oo} a_o(s)^2] \end{aligned} \quad (12)$$

Equation (12) represents the complete closed-loop mathematical model for a translational proof-mass accelerometer. This closed-loop model of the output will reduce to the open-loop model by setting the value of K_f equal to zero.

The SIMULINK block diagram model, created with MATLAB (R2006a), presented in Figure 4 for the translational proof-mass accelerometer can be converted to a complete, working SIMULINK model without a major program effort. Lewis and Kraft (1996) give guidelines for developing such a model which will be useful for accelerometer design, performance studies, and analysis.

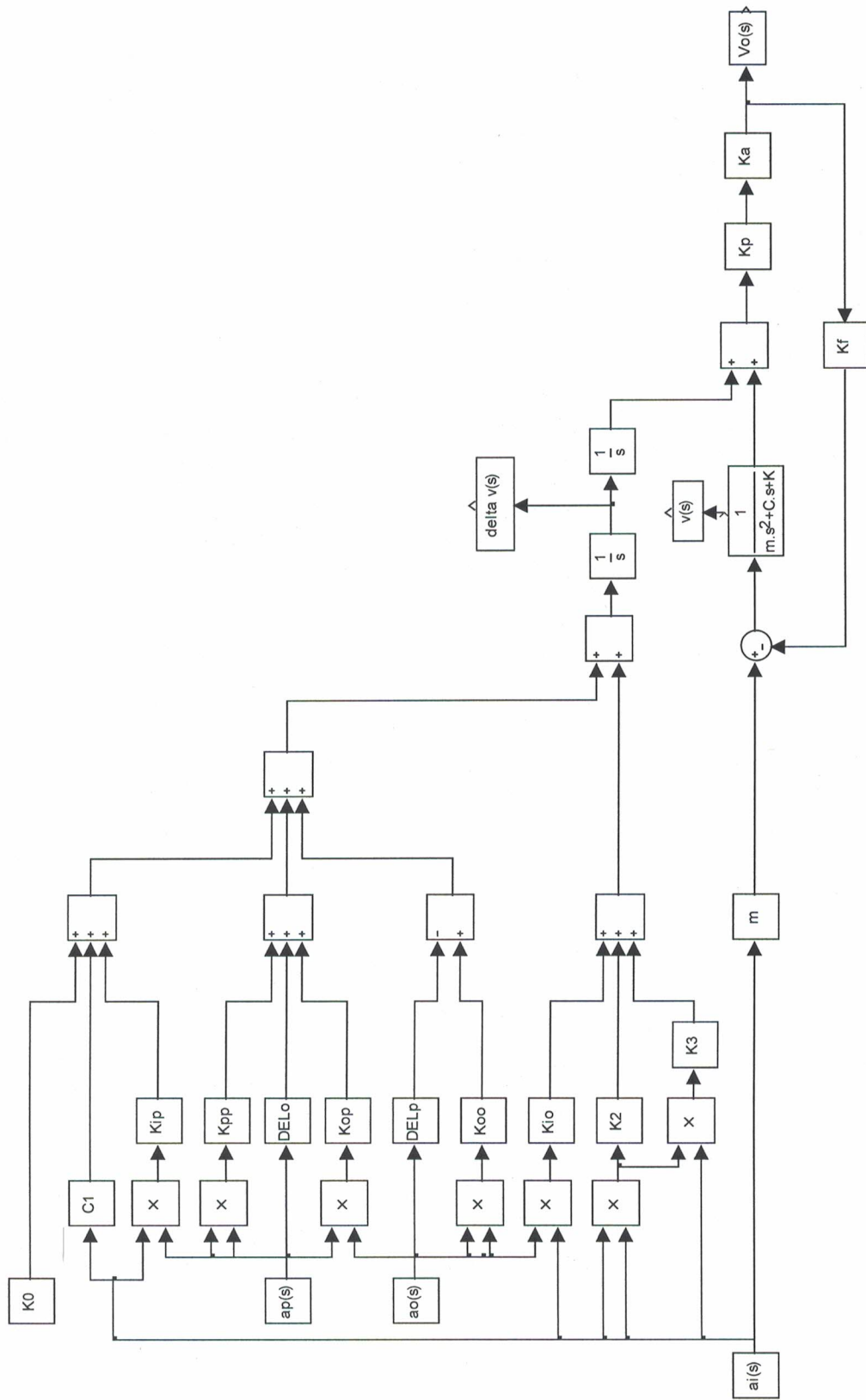


Figure 4. Translational Proof-Mass Accelerometer Closed-Loop Block Diagram

4.2 Pendulous/Torque-Balance Accelerometer

The development of the mathematical model for a pendulous/torque-balance accelerometer is very similar to that of the translational proof-mass accelerometer. This representation is also applicable to vibrating beam accelerometers.

For a typical open-loop pendulous/torque-balance accelerometer, the sensor responds to input acceleration $a(t)$ by a deflection of the pendulum which is proportional to the acceleration. The dynamics of the pendulum can be modeled as a standard rotational spring-mass-damper system. The well-known equations of motion can be written as

$$J\ddot{\theta}(t) + C\dot{\theta}(t) + K_e\theta(t) = T(t) \quad (13)$$

where:

- $\theta(t)$ = angular displacement of the pendulum with respect to the case, rad
- $\dot{\theta}(t)$ = angular velocity of the pendulum with respect to the case, rad/s
- $\ddot{\theta}(t)$ = applied angular acceleration, $a(t)$, of the pendulum with respect to the case, rad/s²
- P = pendulosity, g-cm
- J = mass moment of inertia of the pendulum about the OA axis, g-cm²
- C = damping torque coefficient, dyn-cm/(rad/s)
- K_e = pendulum spring constant, dyn-cm/rad
- T(t) = driving torque, dyn-cm

Taking the Laplace Transform of this equation allows it to be written in the s-plane as

$$[Js^2 + Cs + K_e]\theta(s) = T(s) \quad (14)$$

where:

- s = Laplace operator
- $\theta(s)$ = Laplace Transform of the pendulum angular displacement, $\theta(t)$, rad
- T(s) = Laplace Transform of the driving torque, T(t), dyn-cm

The transformed sensed acceleration, $a(s)$, is converted to the transformed driving torque, T(s), using the relationship

$$T(s) = Pa(s) \quad (15)$$

that is used to generate the output angular displacement, $\theta(s)$. The pickoff and electronics module sense the angular displacement and convert it into a proportional electrical output signal, which can then be approximated by the following equation

$$V_o(s) = K_p K_a \theta(s) \quad (16)$$

where:

- $V_o(s)$ = Laplace Transfer of the output voltage, V
- K_p = pickoff transfer function, V/rad

$$K_a = \text{output amplifier transfer function, } V_{dc}/V_{ac}$$

Combination of Equations (14)-(16) gives the expression for the accelerometer output, $V(s)$, in terms of the input, $a(s)$, as

$$V_o(s) = PK_p K_a a(s) / (Js^2 + Cs + K_e) \quad (17)$$

This represents the standard dynamical open-loop transfer function for a pendulous/torque-balance accelerometer and the corresponding block diagram is shown in Figure 5.

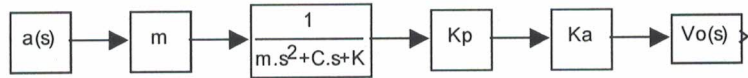


Figure 5. Pendulous/Torque-Balance Accelerometer
Open-Loop Block Diagram (Dynamics-Only)

As discussed by IEEE (1999), accelerometers can provide higher performance for critical applications by use of classical negative feedback, using a torquer acting on the pendulum to minimize the deflection of the pendulum when it is subjected to a torque produced by acceleration of the sensor case. The open-loop model can be converted to a generalized closed-loop model by including a gain, K_t , in the feedback loop. The block diagram for the closed-loop dynamics of a pendulous/torque-balance accelerometer is shown in Figure 6.

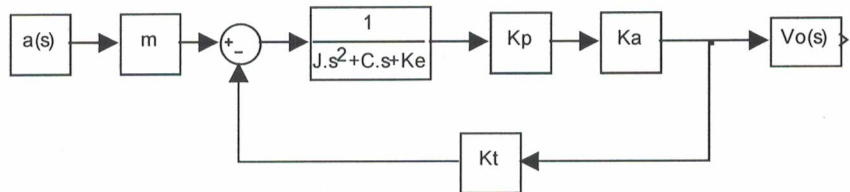


Figure 6. Pendulous/Torque-Balance Accelerometer
Closed-Loop Block Diagram (Dynamics-Only)

Using appropriate block diagram algebra, the accelerometer output for the closed-loop dynamics can be found as

$$V_o(s) = PK_p K_a a(s) / (Js^2 + Cs + K_e + K_f K_p K_a) \quad (18)$$

where K_f = feedback gain, dyn-cm/V

IEEE (1978 and 1999) recommends the use of the same model equation for the pendulous/torque-balance accelerometer as for the translational proof-mass accelerometer using the same model coefficients. Sutherland and Overstreet (2006) present a characterization of the non-linear error terms in a similar model equation. Equations (7)-(10) will therefore also be applicable to pendulous/torque-balance accelerometers and the same reference axes are used.

A SIMULINK block diagram for the complete closed-loop model combining the dynamical model and the error terms for the pendulous/torque-balance accelerometer is shown in Figure 7. Intermediate outputs of velocity are shown for both the dynamic and error models.

Using appropriate block diagram algebra, the accelerometer output can be expressed in terms of the applied accelerations and the error terms as

$$V_o(s) = JK_p K_a a_i(s) / (Js^2 + Cs + K_e + K_f K_p K_a) \\ + K_p K_a (Js^2 + Cs + K_e) \Delta a(s) / [(Js^2 + Cs + K_e + K_f K_p K_a)s^2] \quad (19)$$

Substitution of Equation (10) into Equation (19) will give the expanded form for the accelerometer output as

$$V_o(s) = \{JK_p K_a / (Js^2 + Cs + K_e + K_f K_p K_a) + K_p K_a (Js^2 + Cs + K_e) \\ (C_1 + K_{ip} a_p(s) + K_{io} a_o(s)) / [(Js^2 + Cs + K_e + K_f K_p K_a)s^2]\} a_i(s) \\ + \{K_p K_a (Js^2 + Cs + K_e) / [(Js^2 + Cs + K_e + K_f K_p K_a)s^2]\} \\ [K_2 a_i(s)^2 + K_3 a_i(s)^3 + K_0 + \delta_o a_p(s) - \delta_p a_o(s) + K_{op} a_o(s) a_p(s) \\ + K_{pp} a_p(s)^2 + K_{oo} a_o(s)^2] \quad (20)$$

Equation (20) represents the complete closed-loop mathematical model for a pendulous/torque-balance accelerometer. This closed-loop model of the output will reduce to the open-loop model by setting the value of K_f equal to zero.

The SIMULINK block diagram model presented in Figure 7 for the pendulous/torque-balance accelerometer can be converted to a complete, working SIMULINK model without a major program effort. Again, Lewis and Kraft (1996) give guidelines for developing such a model which will be useful for accelerometer design, performance studies, and analysis.

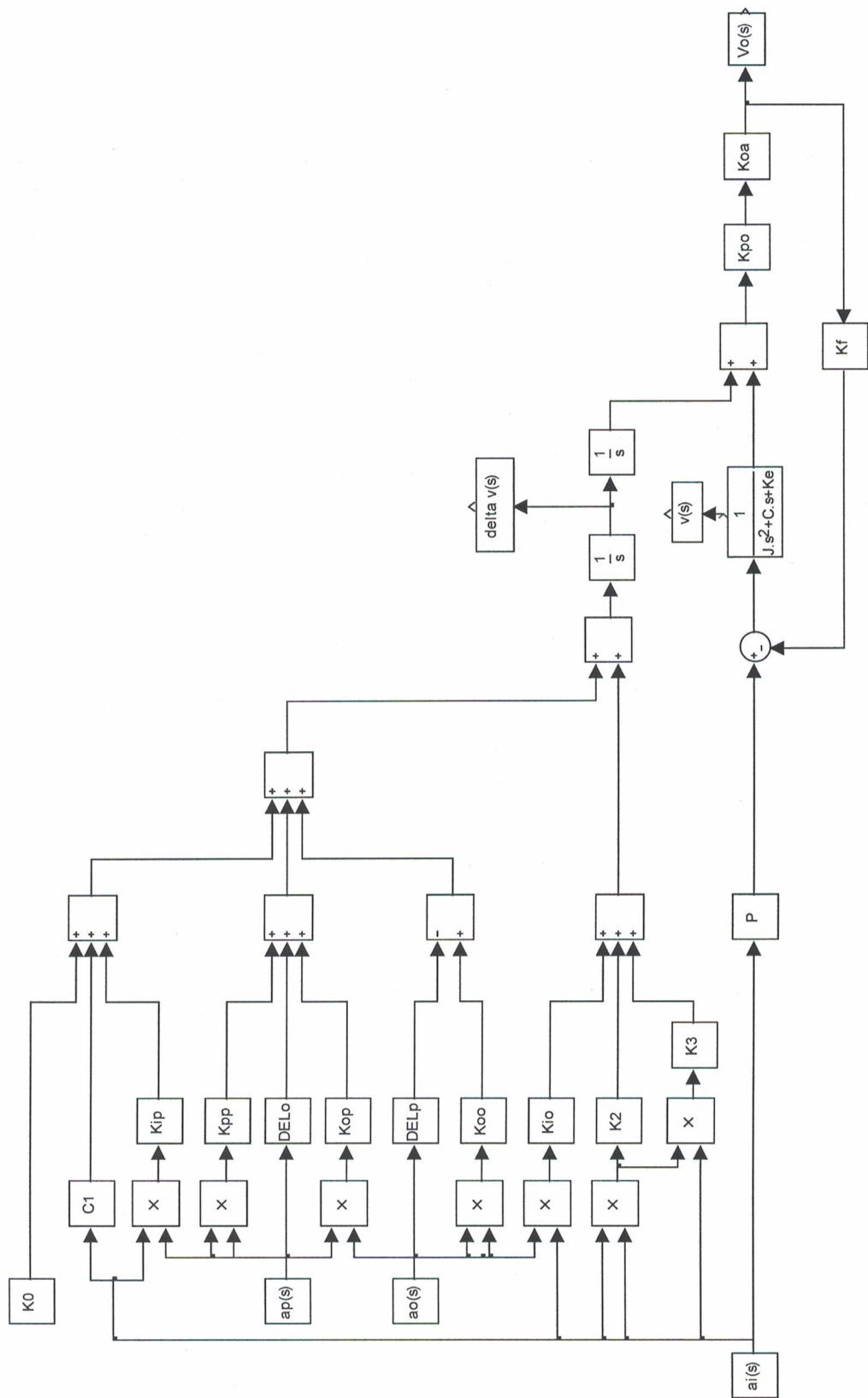


Figure 7. Pendulous/Torque-Balance Accelerometer Closed-Loop Block Diagram

5.0 Gyros

Thielman (2002) and Curey, et al (2004) also provide general descriptions of gyros and their applicable standards. Portions of those discussions are reproduced in this section.

A gyro (gyroscope) is an inertial sensor that measures angular rotation with respect to inertial space about its input axes. The sensing of such motion can utilize the angular momentum of a spinning rotor, the Coriolis effects on a vibrating mass, or the Sagnac effect on counter-propagating light beams in a ring laser or an optical fiber coil.

IEEE (1969(a), and 1969(b)) discuss single-degree-of-freedom spring-restrained rate gyros, while IEEE (1974, and 1980) discuss single-degree-of-freedom rate-integrating spinning-wheel gyros. Spring-restrained rate gyros and rate-integrating gyros are based on the same fundamentals. One of the natural degrees-of-freedom of a spinning wheel is suppressed, and there is a pickoff for sensing motion along the other degree-of-freedom. The pickoff output or the torque required to keep that pickoff at null is the measure of input angular rate sensed by the gyro. Servo control of guidance system gimbals to keep the pickoffs at null for three orthogonal single-degree-of-freedom gyros can also be used to measure the sensed angular rate.

In a ring laser gyro, discussed in IEEE (1996) and in Dorobantu and Gerlach (2004), both clockwise (CW) and counter-clockwise (CCW) propagation of laser light in a polygonal closed gas cavity (three, four, or more sides with mirrors at the vertices) leads to a standing wave(s). Under rotation of the gyro case, the standing wave(s) fixed in inertial space move(s) relative to a photodetector at one of the mirrors, called the Sagnac effect, which thereby provides a measure of the rotation as the wave crests move past the photodetector. The scale factor sensitivity (arcsec per laser wave crest pulse) is inversely proportional to the enclosed area of the closed laser path, so the larger the diameter or path length of the laser resonator cavity, the more sensitive is the laser gyro.

The laser gain medium is helium-neon gas with a high voltage discharge to excite atomic transitions. Piezo-optical or other path length control has to be provided. If operated near zero input angular rates, a technique for preventing lock between the CW and CCW laser beams is required; this can either be mechanical dither of the mounting post, or a magneto-optical means of shifting frequencies and creating multiple laser resonant frequencies.

A fiber optic gyro multiplies the Sagnac effect scale factor by having many repeated turns of an optical fiber around a spindle, so that the longer the fiber length for a given enclosed area, the greater the sensitivity to detecting rotation. An Interferometric Fiber Optic Gyro (IFOG), as described in IEEE (1998), and Chung, et al (2001(a), and 2001(b)), sends laser light through the fiber in both the CW and CCW directions. The interference pattern between the counter-propagating light waves after traversing the fiber is the measure of angular rotation for an open-loop IFOG. A closed-loop IFOG increases the dynamic range of the IFOG with an electro-optic ramping phase bias.

The term Coriolis vibratory gyro (CVG) was created by the Gyro and Accelerometer Panel of the IEEE Aerospace and Electronic Systems Society to describe gyros based on the coupling of a structural, driven, vibrating mode into at least one other structural mode (pickoff) via Coriolis acceleration. These gyro types range from low-cost MEMS devices on silicon or quartz chips to vibrating shell devices, such as the high-performance Hemispherical Resonator Gyro (HRG).

An informative annex in IEEE (2004) gives the principles of operation of these devices, whose dynamic model equations are similar to those of the Foucault pendulum, which can also be regarded as a CVG. Like the Foucault pendulum, there can be a quadrature motion to the desired vibratory motion that must be suppressed by a quadrature control loop in order to have a practical device. Other control loops are for automatic gain control of the drive amplitude and vibration frequency control at the resonant natural frequency. The CVG is termed open-loop if the readout motion is monitored but not controlled, whereas it is termed force-rebalance if the readout motion is nulled.

IEEE (1989), Craig (1972(a), 1972(b), and 1990), and Junqueira and de Barros (2004) discuss two-degree-of-freedom dynamically tuned gyros (DTG). In this gyro design, the spinning wheel is on a shaft with a special hinge. At a certain tuned rotation rate, the spinning wheel becomes as if it has no attachment to the case. There is a certain amount of angular movement that is possible before the spinning wheel hits the gyro stops. Therefore the pickoff of the angular displacement of the wheel relative to the case in two orthogonal directions perpendicular to the wheel spin direction can be used to servo-control guidance system gimbals, to keep the pickoffs at null and the platform on which the DTG is located fixed in inertial space along these axes.

Another method of operation is to use electromagnetic torquing to keep the pickoffs at null, with the amount of torque being the measure of the input angular rates. For a gimbaled guidance system with two DTGs, one pickoff axis on one of the DTGs is caged, i. e., torqued to null, and the other DTG pickoff axes are kept at null with appropriate servo control of the guidance system gimbals.

Mathematical models for the following types of gyros are presented in the section below: spring-restrained rate, rate-integrating, ring laser, interferometric fiber optic, dynamically tuned, and Coriolis vibrating gyros. These mathematical models combine dynamical/physical models and high fidelity error models for each type of accelerometer into a system model represented by SIMULINK block diagrams. The error models contain a number of model parameters which represent different types of possible errors. The number of terms used in the model may be reduced depending on the amount and type of information about the errors that's available for implementation in the model, either from the manufacturer or from testing.

Expressions for the gyro output as functions of the input accelerations, rotation rates, and model parameters are also developed for the system model for both open and

closed-loop representations. Models are presented for single gyros which can be easily converted to a model for a three sensor cluster for implementation into a full IMU model.

5.1 Spring-Restrained Rate Gyro

IEEE (1969(b)) provides a description of the spring-restrained rate gyro addressed in this section. The spring-restrained rate gyro considered is a single degree-of-freedom gyro with an elastic restraint about the output axis. An angular rate about the input axis produces a gyroscopic torque about the output axis that is opposed by a restoring torque exerted by the elastic restraint element. Static equilibrium is reached when the gyroscopic torque about the output axis is exactly balanced by the elastic restraint. The resultant angular rotation of the gimbal relative to the case produces an output signal proportional to the angular rate about the input axis. Output axis damping is generally employed. The spring-restrained rate gyro is normally used as a sensing element to provide electric angular-rate signals in control or indicating systems. The mechanical schematic of a spring-restrained rate gyro is provided in IEEE (1969(a)) and is shown in Figure 8.

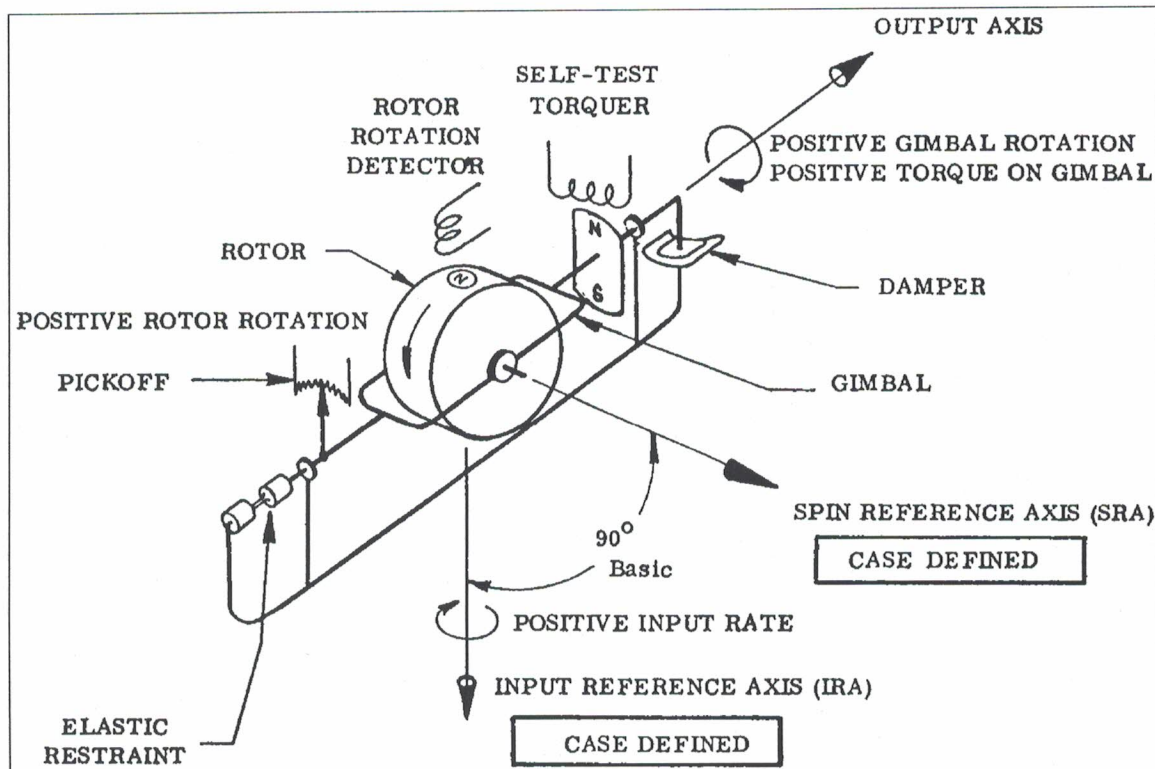


Figure 8. Spring-Restrained Rate Gyro

The dynamics of the spring-restrained rate gyro are also provided by IEEE (1969(a)) and others. With the angular velocity of the case about the IA axis as the input, the equations of motion of this single-degree-of-freedom gyro can be written as

$$(J/H)\ddot{\theta}_o(t) + (C/H)\dot{\theta}_o(t) + (K_r/H)\theta_o(t) = \omega(t) \quad (21)$$

where

- $\theta_o(t)$ = angular displacement of the gimbal about the output axis with respect to the case, rad
- $\dot{\theta}_o(t)$ = angular velocity of the gimbal about the output axis with respect to the case, rad/s
- $\ddot{\theta}_o(t)$ = angular acceleration of the gimbal about the output axis with respect to the case, rad/s²
- J = mass moment of inertia of the gimbal about the output axis, g-cm²
- H = angular momentum of the gimbal about the output axis, g-cm²/s
- C = damping coefficient for gimbal with respect to the gyro case, g-cm²/s
- K_r = restraint spring constant, dyn-cm/rad
- $\omega(t)$ = sensed angular velocity of the gyro case about the IRA axis, rad/s

Taking the Laplace Transform of Equation (21) allows it to be written in the s-plane as

$$[(J/H)s^2 + (C/H)s + (K_r/H)]\theta_o(s) = \omega(s) \quad (22)$$

where:

- s = Laplace operator
- $\theta_o(s)$ = Laplace Transform of the gimbal angular displacement, $\theta_o(t)$, rad
- $\omega(s)$ = Laplace Transform of the sensed case angular velocity, $\omega(t)$, rad/s

Solving Equation (22) for the output $\theta_o(s)$ in terms of the input $\omega(s)$ gives

$$\theta_o(s) = \omega(s) / [(J/H)s^2 + (C/H)s + (K_r/H)] \quad (23)$$

Equation (23) represents the standard dynamical open-loop transfer function for a spring-restrained rate gyro and the corresponding block diagram is shown in Figure 9.

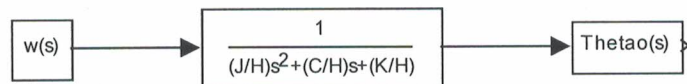


Figure 9. Spring-Restraining Rate Gyro Open-Loop Block Diagram (Dynamics-Only)

The open-loop model can be converted to a generalized closed-loop model by including a gain, K_f , in the feedback loop. The block diagram for the closed-loop dynamics of a spring-restrained rate gyro is shown in Figure 10.

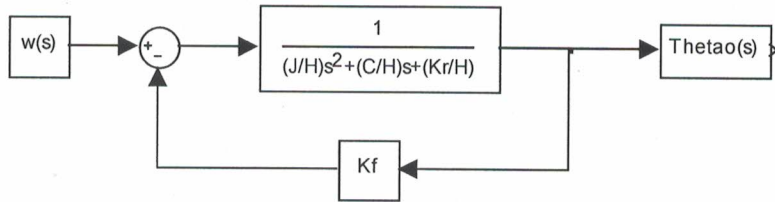


Figure 10. Spring-Restrained Rate Gyro Closed-Loop Block Diagram (Dynamics-Only)

Using appropriate block diagram algebra, the output for the closed-loop dynamics can be found as

$$\theta_o(s) = \omega(s) / [(J/H)s^2 + (C/H)s + (K_r/H) + K_f] \quad (24)$$

where K_f = feedback gain, dyn-cm/rad

IEEE (1969(a)) also provides an error model which consists of a series of terms that mathematically relate the output of the gyro to several acceleration and rate inputs. By including these error terms, the sensed angular velocity of the case for a spring-restrained rate gyro, $\omega(t)$, where all angles are assumed to be small, can be written as

$$\begin{aligned} \omega(t) = & \omega_i(t) - \omega_s(t)\theta_o(t) - \omega_s(t)\varepsilon_o + \omega_o(t)\varepsilon_s - (J/H)\dot{\theta}_o \\ & + D_o + D_{1i}a_i(t) + D_{1s}a_s(t) + D_2a_i(t)a_s(t) + K_t i(t) + \varepsilon(t) \end{aligned} \quad (25)$$

where $\omega_i(t)$, $\omega_s(t)$, $\omega_o(t)$ = applied angular velocities of the gyro case about the IRA, SRA, and output axes, respectively, rad/s

$a_i(t)$, $a_s(t)$ = linear accelerations along the IA and SA axes, respectively, g
 ε_o = misalignment angle between the plane containing the SRA axis and the output axis, and the plane containing the SA axis and the output axis, rad

ε_s = misalignment angle between the plane containing the SA axis and the output axis, and the plane containing the SA and OA axes, rad

D_0 = acceleration-insensitive drift rate (bias), rad/s

D_{1i} = acceleration-sensitive drift rate coefficient for $a_i(t)$, rad/s-g

D_{1s} = acceleration-sensitive drift rate coefficient for $a_s(t)$, rad/s-g

D_2 = acceleration-squared-sensitive drift rate coefficient, rad/s-g²

K_t = command rate scale factor, rad/s-A

$i(t)$ = torquer command current, A

$\varepsilon(t)$ = random measurement and process noise, rad/s

As with accelerometers, the bias and axis misalignment modeling coefficients can often be obtained from the manufacturer's specification sheets for commercially available gyros. The values of the other modeling coefficients are generally not available from the manufacturer and must be obtained through testing and calibration of each unit. Additional information regarding the mathematical form, physical meaning, and procedures for accelerometer testing and calibration is provided by the IEEE (1969(a) and 1969(b)). Upon performing the specified tests, the method of least squares can be used to determine the values of the model coefficients using the data obtained in the testing program.

Once again, the random measurement and process noise can be modeled in a guidance system Kalman filter model using augmented Markov process states. As a result, the random process noise will not appear in the model equation upon taking the Laplace Transform of Equation (25), which gives the result

$$\begin{aligned}\omega(s) = & \omega_i(s) - \omega_s(s)(\theta_o(s) + \varepsilon_o) + \omega_o(s)\varepsilon_s - (J/H)_o \\ & + D_o + D_{1i}a_i(s) + D_{1s}a_s(s) + D_2a_i(s)a_s(s) + K_t i(s)\end{aligned}\quad (26)$$

Equation (26) can be written as the sum of the applied angular velocity of the case about the IRA axis and error terms in the sensed angular velocity due to the gyro performance as

$$\omega(s) = \omega_i(s) + \Delta\omega(s) - \omega_s(s)\theta_o(s) \quad (27)$$

where

$$\begin{aligned}\Delta\omega(s) = & -\omega_s(s)\varepsilon_o + \omega_o(s)\varepsilon_s - (J/H)_o + D_o \\ & + D_{1i}a_i(s) + D_{1s}a_s(s) + D_2a_i(s)a_s(s) + K_t i(s)\end{aligned}\quad (28)$$

This representation will allow direct integration of the error terms separate from the dynamics which will result in a more accurate model. Since the right side of Equation (28) is a function of $\theta_o(s)$, the appropriate block diagram algebra can develop an expression for the gyro output in terms of the applied accelerations and rotation rates and the error terms as

$$\theta_o(s) = [\omega_i(s) + \Delta\omega(s)] / [(J/H)s^2 + (C/H)s + (K_r/H) + K_f + \omega_s(s)] \quad (29)$$

Substitution of Equation (28) into Equation (29) will give the expanded form for the gyro output as

$$\begin{aligned}\theta_o(s) = & [\omega_i(s) - \omega_s(s)\varepsilon_o + \omega_o(s)\varepsilon_s - (J/H)_o + D_o \\ & + D_{1i}a_i(s) + D_{1s}a_s(s) + D_2a_i(s)a_s(s) + K_t i(s)] \\ & / [(J/H)s^2 + (C/H)s + (K_r/H) + K_f + \omega_s(s)]\end{aligned}\quad (30)$$

Equation (30) represents the complete closed-loop mathematical model for a spring-restrained rate gyro. This closed-loop model of the output will reduce to the open-loop model by setting the value of K_f equal to zero.

The SIMULINK block diagram model is presented in Figure 11 for the spring-restrained rate gyro. This model can also be converted to a complete, working SIMULINK model without a major program effort.

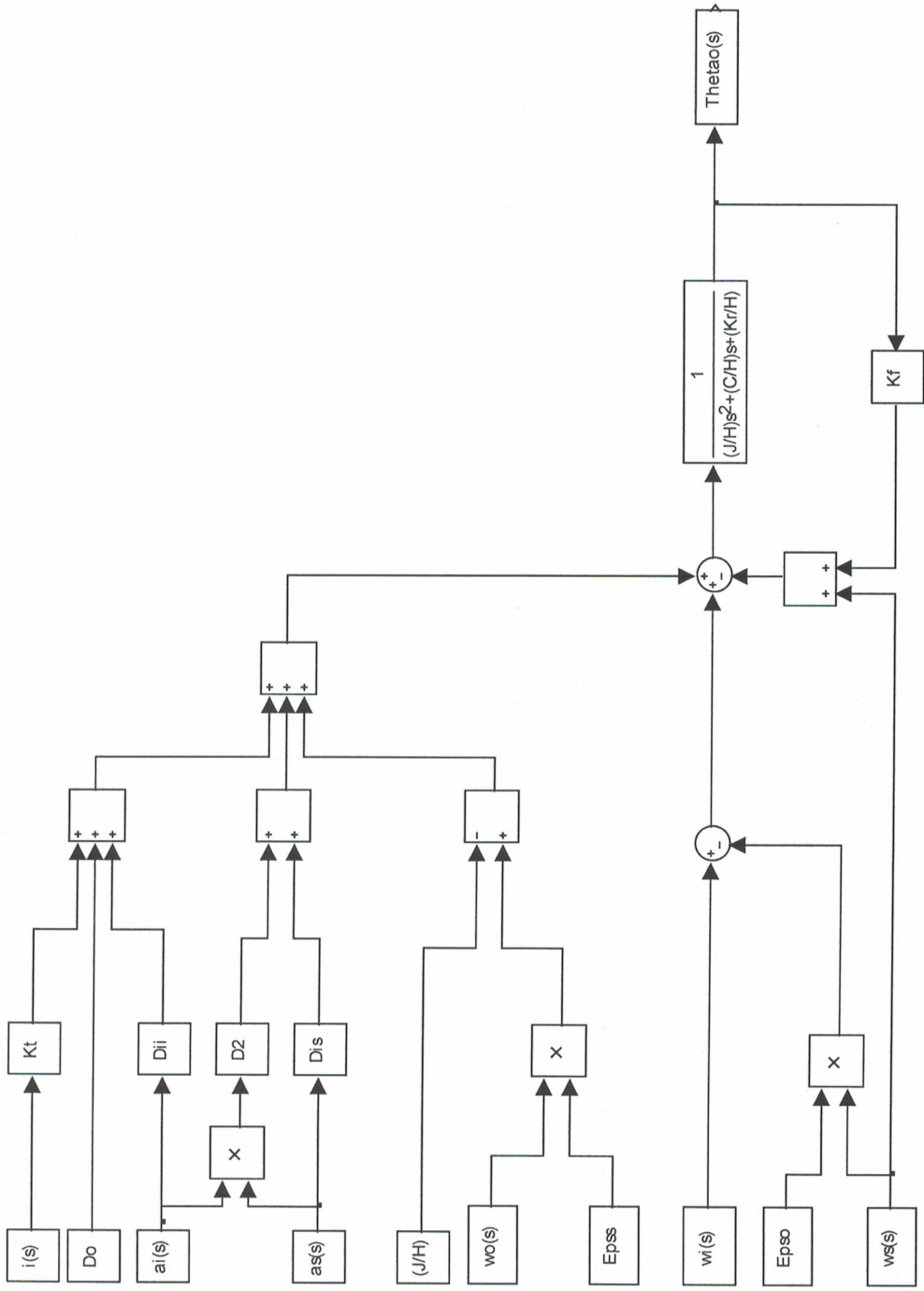


Figure 11. Spring-Restrained Rate Gyro Closed-Loop Block Diagram

5.2 Rate-Integrating Gyro

The development of a mathematical model for a rate-integrating gyro in this section closely follows that of a spring-restrained rate gyro and will employ the same coordinate system as shown in Figure 8. IEEE (1974) provides standard specifications for a single degree-of-freedom rate-integrating gyro, and IEEE (1980) provides a supplement for strapdown applications of a rate-integrating gyro. While the models presented are similar, the more general model described for strapdown applications will be considered in this section. Craig (1972(a), 1972(b), and 1990) and Junqueira and de Barros (2004) also present discussion and derivation of similar dynamical models.

The dynamics of the rate-integrating rate gyro are modeled with the angular velocity of the case about the IRA axis as the input. The equations of motion of this single-degree-of-freedom gyro can be written as

$$(J_o / H + \tau_\alpha)(\ddot{\theta}_o(t) + \ddot{\phi}_o(t)) + (C / H)\dot{\theta}_o(t) + (K / H)\theta_o(t) = \omega(t) \quad (31)$$

- where
- $\theta_o(t)$ = angular displacement of the gimbal about the output axis with respect to the case, rad
 - $\dot{\theta}_o(t)$ = angular velocity of the gimbal about the output axis with respect to the case, rad/s
 - $\ddot{\theta}_o(t)$ = angular acceleration of the gimbal about the output axis with respect to the case, rad/s²
 - $\ddot{\phi}_o(t)$ = angular acceleration of the case about the output axis with respect to inertial space, rad/s²
 - J_i, J_o, J_s = mass moment of inertia of the gimbal about the input, output, and spin axes, respectively, g-cm²
 - H = angular momentum of the rotor, g-cm²/s
 - τ_α = time constant increment due to fluid mass coupling, s
 - C = damping coefficient about the output axis with respect to the case, g-cm²/s
 - K = spring constant about the output axis with respect to the case, dyn-cm/rad
 - $\omega(t)$ = sensed angular velocity of the case about the input axis, rad/s

Taking the Laplace Transform of Equation (31) allows it to be written in the s-plane as

$$(J_o / H + \tau_\alpha)(s^2\theta_o(s) + s^2\phi_o(s)) + (C / H)s\theta_o(s) + (K / H)\theta_o(s) = \omega(s) \quad (32)$$

- where:
- s = Laplace operator
 - $\theta_o(s)$ = Laplace Transform of the gimbal angular displacement about the output axis with respect to the case, $\theta_o(t)$, rad

$\phi_o(s)$ = Laplace Transform of the case angular displacement about the output axis with respect to inertial space, $\phi_o(t)$, rad

$\omega(s)$ = Laplace Transform of the sensed case angular velocity about the input axis, $\omega(t)$, rad/s

Solving Equation (32) for the output $\theta_o(s)$ in terms of the input $\omega(s)$ gives

$$\theta_o(s) = \frac{[\omega(s) - (J_o/H + \tau_\alpha)s^2\phi_o(s)]}{[(J_o/H + \tau_\alpha)s^2 + (C/H)s + (K/H)]} \quad (33)$$

Equation (33) represents the standard dynamical open-loop transfer function for a rate-integrating gyro and the corresponding block diagram is shown in Figure 12.

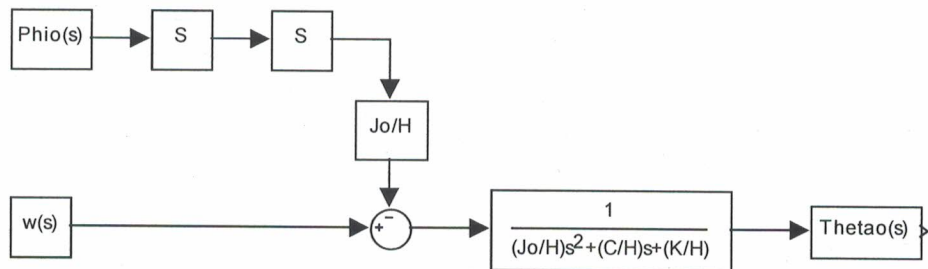


Figure 12. Rate-Integrating Gyro Open-Loop
Block Diagram (Dynamics-Only)

The open-loop model can also be converted to a generalized closed-loop model by including a gain, K_f , in the feedback loop. The block diagram for the closed-loop dynamics of a spring-restrained rate gyro is shown in Figure 13.

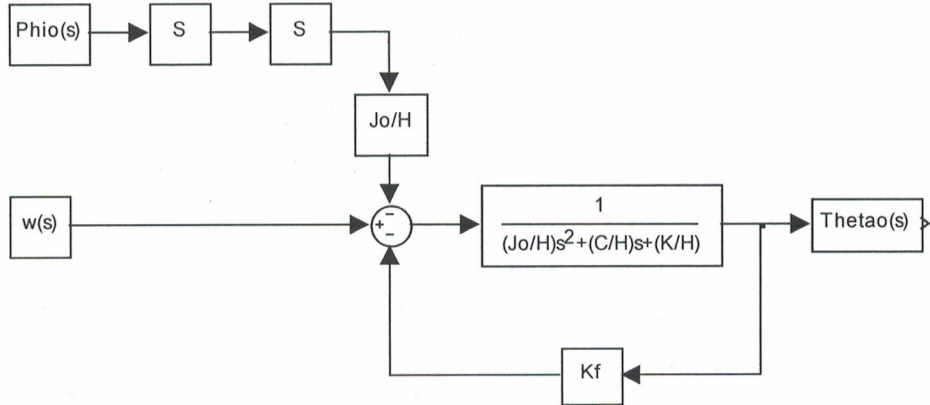


Figure 13. Rate-Integrating Gyro Closed-Loop Block Diagram (Dynamics-Only)

Using appropriate block diagram algebra, the output for the closed-loop dynamics can be found as

$$\theta_o(s) = [\omega(s) - (J_o / H + \tau_\alpha) s^2 \phi_o(s)] / [(J_o / H + \tau_\alpha) s^2 + (C / H) s + (K / H) + K_f] \quad (34)$$

where K_f = feedback gain, dyn-cm/rad

IEEE (1980) also provides an error model which consists of a series of terms that mathematically relate the output of the gyro to several acceleration and rate inputs. By including these error terms and the assumption that all angles are assumed to be small, the sensed angular velocity of the case for a rate-integrating gyro, $\omega(t)$, can be written as

$$\begin{aligned} \omega(t) = & \omega_i(t) - \omega_s(t)\theta_o(t) + D_f + D_i a_i(t) + D_o a_o(t) + D_s a_s(t) \\ & + D_{ii} a_i(t)^2 + D_{ss} a_s(t)^2 + D_{is} a_i(t) a_s(t) + D_{io} a_i(t) a_o(t) \\ & + D_{os} a_o(t) a_s(t) + [(J_s - J_i) / H] \omega_i(t) \omega_s(t) + D_\omega + K_i i(t) + \varepsilon(t) \end{aligned} \quad (35)$$

where $\omega_i(t)$, $\omega_o(t)$, $\omega_s(t)$ = applied angular velocities of the gyro case about the input, output, and spin axes, respectively, rad/s

$a_i(t)$, $a_o(t)$, $a_s(t)$ = linear accelerations along the input, output, and spin axes, respectively, g

D_f = acceleration-insensitive drift rate (bias), rad/s

D_i , D_o , D_s = acceleration-sensitive drift rate coefficients for $a_i(t)$, $a_o(t)$, and $a_s(t)$, respectively, rad/s-g

D_{ii} = acceleration-sensitive drift rate coefficient for $a_i(t)^2$, rad/s-g²

D_{ss} = acceleration-sensitive drift rate coefficient for $a_s(t)^2$, rad/s-g²

D_{is} = acceleration-sensitive drift rate coefficient for $a_i(t) a_s(t)$, rad/s-g²

D_{io} = acceleration-sensitive drift rate coefficient for $a_i(t)$ $a_o(t)$, rad/s-g²
 D_{os} = acceleration-sensitive drift rate coefficient for $a_o(t)$ $a_s(t)$, rad/s-g²
 D_o = rate error due to angular rate about the output axis which is a function of ω_o , rad/s
 K_t = command rate scale factor, rad/s-A
 $i(t)$ = torquer command current, A
 $\varepsilon(t)$ = random measurement and process noise, rad/s

The bias and axis misalignment modeling coefficients can often be obtained from the manufacturer's specification sheets for commercially available gyros. The values of the other coefficients are generally not available from the manufacturer and must be obtained through testing and calibration of each unit. Additional information regarding the mathematical form, physical meaning, and procedures for accelerometer testing and calibration is provided by the IEEE (1974 and 1980). Upon performing the specified tests, the method of least squares can be used to determine the values of the model coefficients using the data obtained in the testing program.

As described earlier, the random measurement and process noise can be modeled in a guidance system Kalman filter model using augmented Markov process states and will not appear in the model equation upon taking the Laplace Transform of Equation (35), which gives the result

$$\begin{aligned}
 \omega(s) = & \omega_i(s) - \omega_s(s)\theta_o(s) + D_f + D_i a_i(s) + D_o a_o(s) + D_s a_s(s) \\
 & + D_{ii} a_i(s)^2 + D_{ss} a_s(s)^2 + D_{is} a_i(s)a_s(s) + D_{io} a_i(s)a_o(s) \\
 & + D_{os} a_o(s)a_s(s) + [(J_s - J_i)/H]\omega_i(s)\omega_s(s) + D_\omega + K_t i(s)
 \end{aligned} \tag{36}$$

Equation (36) can be written as the sum of the applied angular velocity of the case about the input axis and error terms in the sensed angular velocity due to the gyro performance as

$$\omega(s) = \omega_i(s) + \Delta\omega(s) - \omega_s(s)\theta_o(s) \tag{37}$$

where

$$\begin{aligned}
 \Delta\omega(s) = & D_f + D_i a_i(s) + D_o a_o(s) + D_s a_s(s) \\
 & + D_{ii} a_i(s)^2 + D_{ss} a_s(s)^2 + D_{is} a_i(s)a_s(s) + D_{io} a_i(s)a_o(s) \\
 & + D_{os} a_o(s)a_s(s) + [(J_s - J_i)/H]\omega_i(s)\omega_s(s) + D_\omega + K_t i(s)
 \end{aligned} \tag{38}$$

This representation will allow direct integration of the error terms separate from the dynamics which will result in a more accurate model. A SIMULINK block diagram for the complete model combining the dynamical model and the error terms is shown in Figure 14.

Since the right side of Equation (38) is a function of $\theta_o(s)$, the appropriate block diagram algebra can develop an expression for the gyro output in terms of the applied accelerations and rotation rates and the error terms as

$$\begin{aligned}\theta_o(s) = & [\omega_i(s) - (J_o/H + \tau_\alpha)s^2\phi_o(s) + \Delta\omega(s)] \\ & /[(J_o/H + \tau_\alpha)s^2 + (C/H)s + (K/H) + K_f + \omega_s(s)]\end{aligned}\quad (39)$$

Substitution of Equation (38) into Equation (39) will give the expanded form for the gyro output as

$$\begin{aligned}\theta_o(s) = & [\omega_i(s) - (J_o/H + \tau_\alpha)s^2\phi_o(s) + D_f + D_i a_i(s) + D_o a_o(s) \\ & + D_s a_s(s) + D_{ii} a_i(s)^2 + D_{ss} a_s(s)^2 + D_{is} a_i(s)a_s(s) + D_{io} a_i(s)a_o(s) \\ & + D_{os} a_o(s)a_s(s) + [(J_s - J_i)/H]\omega_i(s)\omega_s(s) + D_\omega + K_t i(s)] \\ & /[(J_o/H + \tau_\alpha)s^2 + (C/H)s + (K/H) + K_f + \omega_s(s)]\end{aligned}\quad (40)$$

Equation (40) represents the complete closed-loop mathematical model for a rate-integrating gyro. This closed-loop model of the output will reduce to the open-loop model by setting the value of K_f equal to zero.

The SIMULINK block diagram model presented in Figure 14 for the rate-integrating rate gyro can also be converted to a complete, working SIMULINK model without a major program effort.

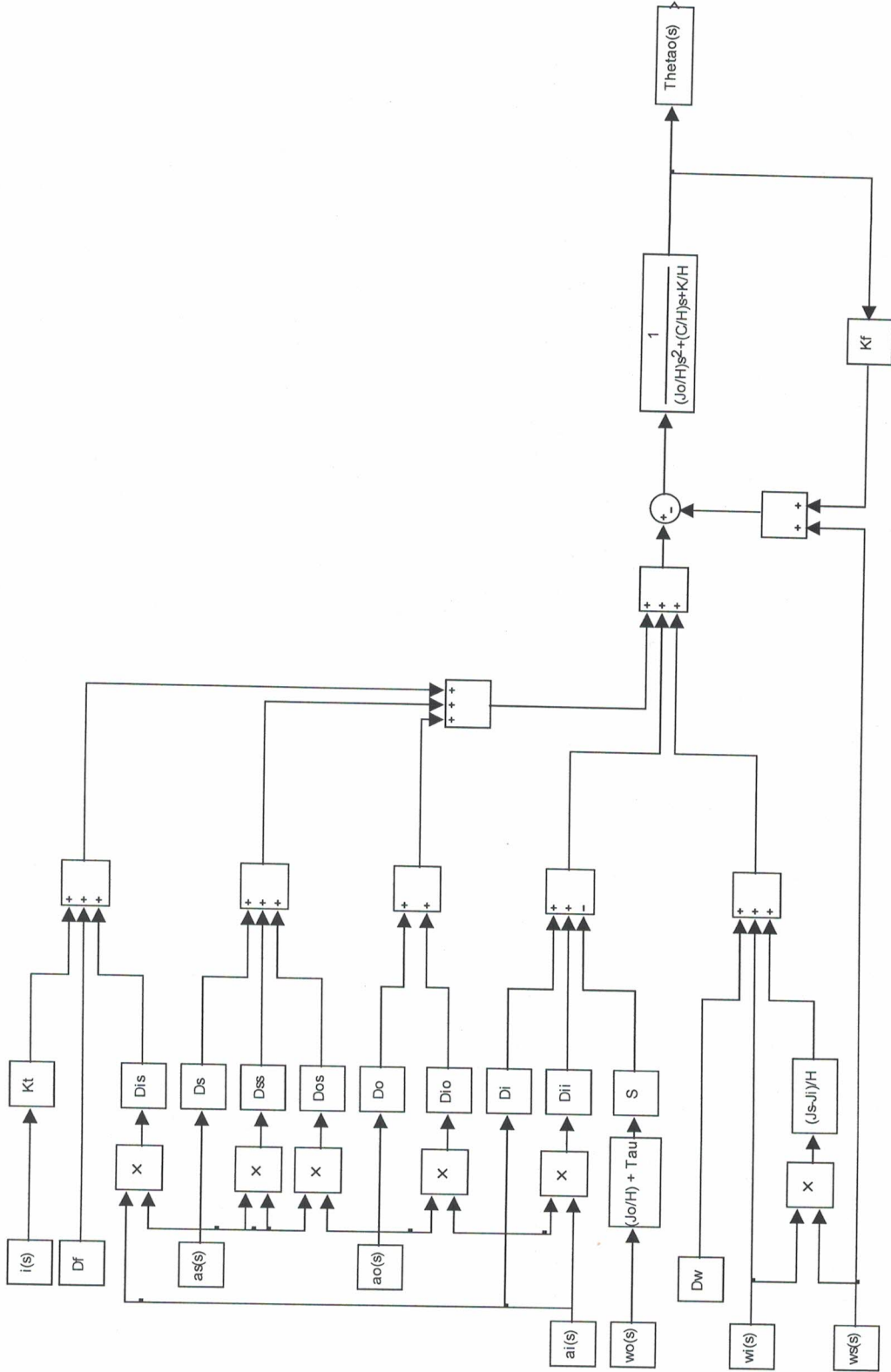


Figure 14. Rate-Integrating Gyro Closed-Loop Block Diagram

5.3 Ring Laser Gyro

The principle of operation of a ring laser gyro is very different from that of the more conventional rate and rate-integrating gyros. Ring laser gyros use the propagation of laser light in an enclosed cavity and the Sagnac effect to measure the rotation rate of the gyro case. Sharp (2000) and Dorobantu and Gerlach (2004) provide reviews of the principles upon which a ring laser gyro is based and are used in the discussion below.

Ring lasers use two laser beams circulating in opposite directions within an enclosed cavity. The cavity is generally in the form of an equilateral triangle and the beams travel the triangular path with a known frequency. When the cavity is rotated, there is a difference in the path length for the two counter propagating beams. Combination of the two output beams creates an interference pattern which is modulated by a beat frequency which is proportional to the rate of rotation of the gyro case. This relationship between the beat frequency, or pulse rate, and the applied rotation rate to the gyro case can be written as

$$f(t) = 4\omega(t)A / \lambda L \quad (41)$$

where

$f(t)$ = pulse rate, pulse/s

$\omega(t)$ = sensed angular velocity of gyro case, arcsec/s

A = area of equilateral triangle formed by enclosed cavity, cm²

λ = wavelength of laser beam, cm

L = perimeter of equilateral triangle, cm

As shown in Equation (41), the relationship between the rotation rate input and the pulse rate output is purely algebraic and is not described using the laws of dynamics. This will eliminate the need to use a dynamical model to describe the performance of a ring laser gyro, and the angular position of the gyro case can be obtained simply by integrating the sensed angular velocity.

Taking the Laplace Transform of Equation (41) allows it to be written in the s-plane as

$$f(s) = 4\omega(s)A / \lambda L \quad (42)$$

where

s = Laplace operator

$f(s)$ = Laplace Transform of the pulse rate, $f(t)$, pulse/s

$\omega(s)$ = Laplace Transform of the sensed angular velocity, $\omega(t)$, rad/s

The open-loop model of this relationship is shown in Figure 15. Since this model is not dynamical in nature and there are no errors included yet, there is no closed-loop system representation.

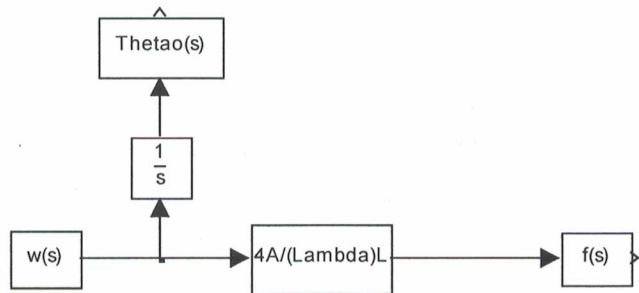


Figure 15. Ring Laser Gyro Open-Loop Block Diagram (No Errors)

This actual sensed angular velocity will be a combination of the applied angular velocity and any corrupting errors which are present in the physical system. IEEE (1996) provides standard specifications and testing procedures for a ring laser gyro as well as a model equation of a gyro which models possible error sources as a series of terms that mathematically relate ring laser output, $f(t)$, to the input of the applied angular velocities and coefficients modeling physical parameters of the laser.

The coordinate system defined for this ring laser model equation is provided in Figure 16 below, which also shows the axis misalignment angles θ_N and θ_L .

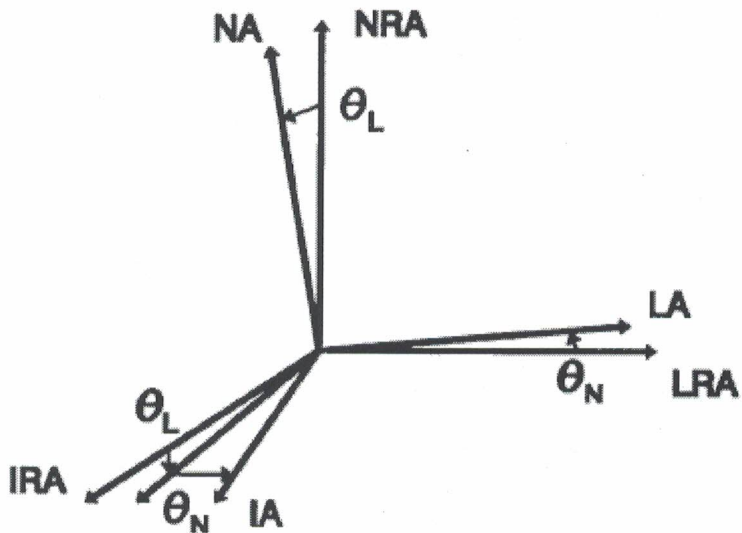


Figure 16. Ring Laser Gyro Coordinate System and Misalignment Angles

The model equation is provided as

$$K_0 f(t) = [\omega(t) + E(t) + D(t)]/[1 + 10^{-6} \varepsilon_k(t)] + \varepsilon(t) \quad (43)$$

where K_0 = nominal scale factor, arcsec/pulse
 $E(t)$ = environmentally sensitive error terms, arcsec/s
 $D(t)$ = drift terms, arcsec/s
 $\varepsilon_k(t)$ = scale factor error, ppm
 $\varepsilon(t)$ = random measurement and process noise, arcsec/s

Also, the individual terms in Equation (43) are further defined as

$$K_0 = \lambda L / 4A \quad (44)$$

$$\omega(t) = \omega_I(t) + \omega_L(t) \sin \theta_N - \omega_N(t) \sin \theta_L \quad (45)$$

$$E(t) = D_T \Delta T(t) + D_{GRADT} GRADT(t) \quad (46)$$

$$D(t) = D_F + D_F(t) + D_{RN} + D_{RB} + D_{RK} + D_{RR} + D_Q \quad (47)$$

$$\varepsilon_k(t) = \varepsilon_T \Delta T(t) + \varepsilon_{GRADT} GRADT(t) + f_{\omega l} \quad (48)$$

where $\omega_I(t)$, $\omega_N(t)$, $\omega_L(t)$ = applied angular velocities about the IRA, NRA, and LRA axes, respectively, arcsec/s

θ_N , θ_L = misalignment of the IA axis about the NRA and LRA axes, respectively, arcsec
 D_T = drift rate temperature sensitivity coefficient, arcsec/s-°
 D_{GRADT} = coefficient vector of temperature gradient drift rate sensitivity vector, arcsec-cm/s-°
 ΔT = temperature change, °
 $GRADT$ = gradient of the temperature, °/cm
 D_F = bias, arcsec/s
 $D_F(t)$ = variations in bias during warm-up period, arcsec/s
 D_{RN} = random drift rate due to angle random walk, arcsec/s
 D_{RB} = random drift rate due to bias instability, arcsec/s
 D_{RK} = random drift rate due to rate random walk, arcsec/s
 D_{RR} = random drift rate due to rate ramp, arcsec/s
 D_Q = combined effect of apparent equivalent random drift rate due to angle quantization, and the apparent equivalent random drift rate due to the anti-lock residual, random drift rate from angle random walk, arcsec/s
 ε_T = scale factor temperature sensitivity coefficient, ppm/°
 ε_{GRADT} = coefficient vector of the temperature gradient scale factor sensitivity, ppm-cm/°
 $f_{\omega l}$ = scale factor nonlinearity, ppm

Substitution of Equations (44)-(48) into Equation (43) yields

$$\begin{aligned} K_0 f(t) = & [\omega_I(t) + \omega_L(t) \sin \theta_N - \omega_N(t) \sin \theta_L + D_T \Delta T \\ & + D_{GRADT} GRADT + D_F + D_F(t) + D_{RN} + D_{RB} + D_{RK} + D_{RR} \\ & + D_Q] / [1 + 10^{-6} (\varepsilon_T \Delta T + \varepsilon_{GRADT} GRADT + f_{\omega l})] + \varepsilon(t) \end{aligned} \quad (49)$$

Taking the Laplace Transform of Equation (49) gives the model equation in the s-plane in terms of the applied angular velocities and model coefficients, from which a SIMULINK block diagram can be constructed, as

$$\begin{aligned} K_0 f(s) = & [\omega_I(s) + \omega_L(s) \sin \theta_N - \omega_N(s) \sin \theta_L + D_T \Delta T \\ & + D_{GRADT} GRADT + D_F + D_F(s) + D_{RN} + D_{RB} + D_{RK} + D_{RR} \\ & + D_Q] / [1 + 10^{-6} (\varepsilon_T \Delta T + \varepsilon_{GRADT} GRADT + f_{\omega l})] \end{aligned} \quad (50)$$

It should be noted that the right side of Equation (50) represents the sensed rotation rate of the gyro, and integration of the right side will provide the angular position using the relationship

$$s \theta_o(s) = \omega(s) \quad (51)$$

Further, the solution of Equation (50) for $f(s)$ will yield the pulse rate of the gyro. Both can be done within the block diagram model.

IEEE (1996) recommends a simple closed-loop block diagram in the development of Equation (43). Application of the same block diagram for use with Equation (50) produces the complete mathematical model for a ring laser gyro. This model is provided in Figure 17 below. Using the block diagram to solve for the angular position gives

$$\begin{aligned} \theta_o(s) = & [\omega_I(s) + \omega_L(s) \sin \theta_N - \omega_N(s) \sin \theta_L + D_T \Delta T \\ & + D_{GRADT} GRADT + D_F + D_F(s) + D_{RN} + D_{RB} + D_{RK} + D_{RR} \\ & + D_Q] / s[1 + 10^{-6} (\varepsilon_T \Delta T + \varepsilon_{GRADT} GRADT + f_{\omega l})] \end{aligned} \quad (51)$$

Again, the SIMULINK block diagram model for the ring laser gyro can be converted to a complete, working SIMULINK model without a major program effort.

For ring laser gyros, manufacturer's specification sheets often provide information regarding bias, axis misalignment, scale factor nonlinearity, angle random walk, and rate random walk which could be used directly in the model. The other model coefficients must be obtained through testing procedures.

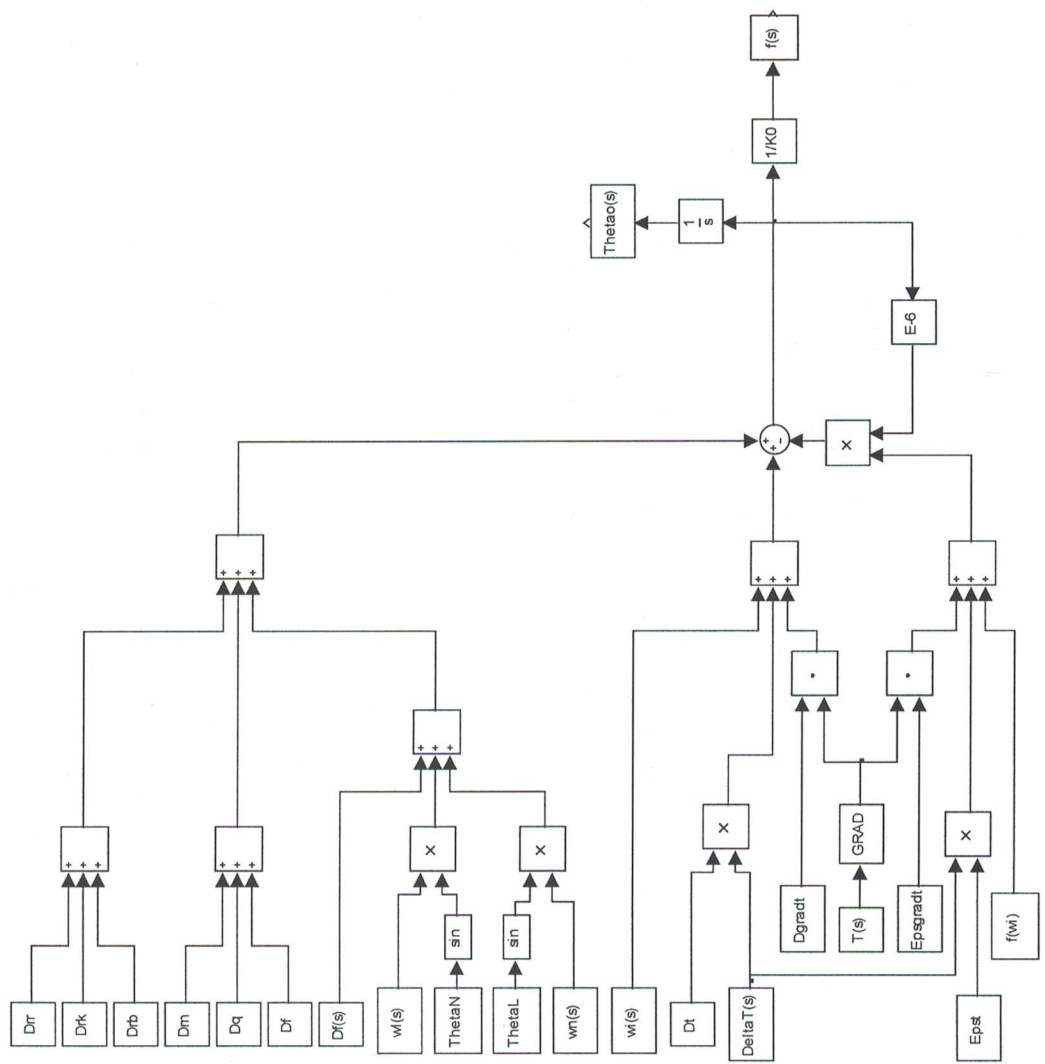


Figure 17. Ring Laser Gyro Closed-Loop Block Diagram

As discussed by Dorobantu and Gerlach (2004), the major drawback to use of a ring laser gyro is the “lock-in” effect. This occurs as a consequence of the coupling of the two CW and CCW laser beams with closely oscillating frequencies inside the resonant cavity. The coupling is principally due to the back-scattering on the mirror levels by the reciprocal energy injection from one wave to the other. Therefore, the mirror quality is a key factor in the performance of a ring laser gyro.

The lock-in effect can be overcome by the use of a symmetrically mechanical oscillation rate, or dither, in order to modify the cavity refraction index. This mechanical dither signal is then eliminated from the gyroscope output signal. However, the use of a randomized sinusoidal dither to overcome the lock-in effect also introduces an additional component of angular random walk noise (ARW) into the measurement process. Aronowitz (1999) and Dorobantu and Gerlach (2004) express this noise as an uncertainty in the angle measurement as

$$\delta ARW = \Omega_{L_I} \sqrt{K_0 / 2\pi\Omega_D} \quad (52)$$

where Ω_{L_I} = lock-in rate, arcsec/s
 Ω_D = dither angular velocity, arcsec/s

This angular random walk noise can be accounted for the mathematical model of the laser ring gyro by inclusion of Equation (52) into the modeling equation. This can be done by first taking the Laplace Transform of Equation (52) then including this transformed term into the series of error terms in Equation (51).

5.4 Interferometric Fiber Optic Gyro (IFOG)

A fiber optic gyro also relies on the Sagnac effect with which to detect rotational motion. It uses an optical fiber wound in many repeated circular turns to create a longer fiber length which results in the multiplication of the Sagnac effect scale factor. The standard specifications and test procedures are presented by IEEE (1998) for single-axis IFOGs. Modeling and calibration of IFOGs are also discussed by Chung, et al (2001(a) and 2001(b)).

The corresponding model equation for an IFOG provided by IEEE (1998) is nearly identical to the model equation for a ring laser gyro, with slight variation in several error source terms. Therefore, Equations (41) and (42) will also apply to IFOGs and the open-loop transfer function will be the same one shown in Figure 15 for a ring laser gyro, which is shown here again as Figure 18 for completeness.

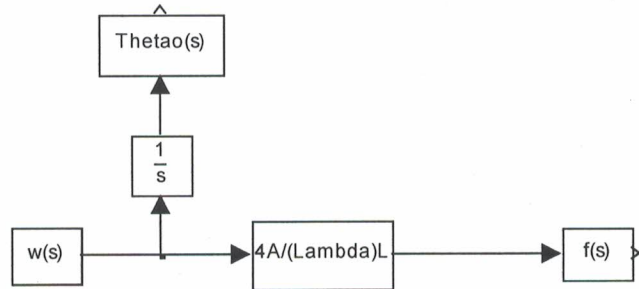


Figure 18. Interferometric Fiber Optic Gyro Open-Loop Block Diagram (No Errors)

The coordinate system defined for this IFOG model equation is provided in Figure 19 below, which also shows the axis misalignment angles θ_N and θ_L .

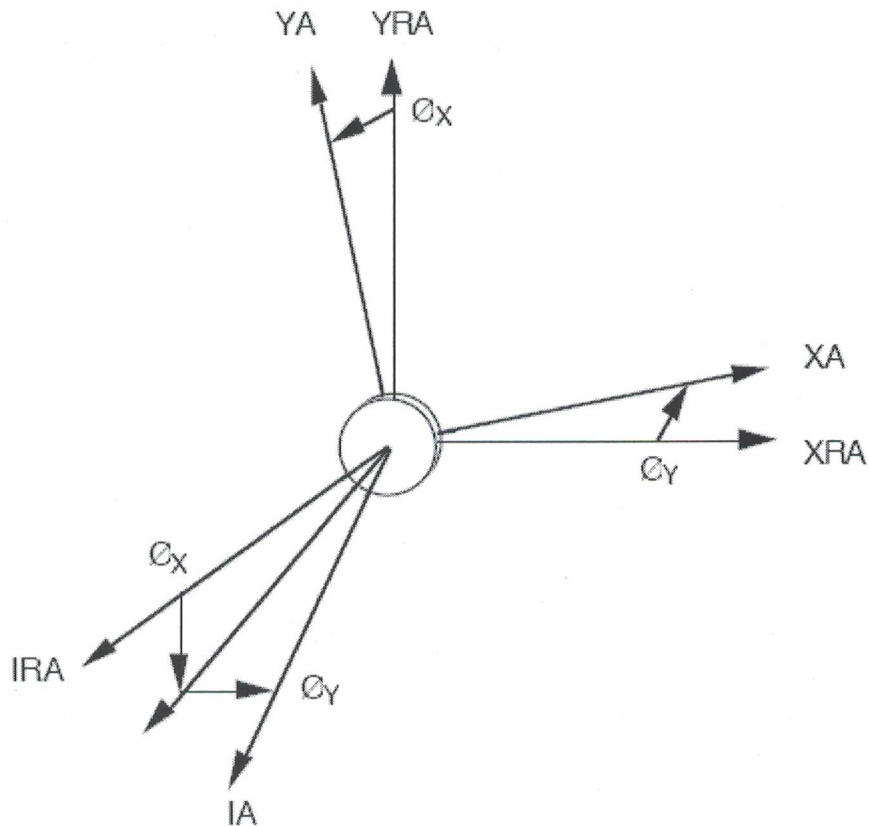


Figure 19. Interferometric Fiber Optic Gyro Coordinate System and Misalignment Angles

Equations (43) and (44) will also apply to the IFOG and will be repeated here as Equations (53) and (54). However, Equations (45)-(48) will be modified to include different error sources according to the recommendations provided in IEEE (1998) as shown below.

$$K_0 f(t) = [\omega(t) + E(t) + D(t)]/[1 + 10^{-6} \varepsilon_k(t)] + \varepsilon(t) \quad (53)$$

where

- K_0 = nominal scale factor, deg/pulse
- $f(t)$ = pulse rate, pulse/s
- $\omega(t)$ = sensed angular velocity of gyro case, deg/s
- $E(t)$ = environmentally sensitive error terms, deg/s
- $D(t)$ = drift terms, deg/s
- $\varepsilon_k(t)$ = scale factor error, ppm
- $\varepsilon(t)$ = random measurement and process noise, deg/s

Also, the individual terms in Equation (53) are further defined as

$$K_0 = \lambda L / 4A \quad (54)$$

$$\omega(t) = \omega_{IRA}(t) + \omega_{XRA}(t) \sin \theta_Y - \omega_{YRA}(t) \sin \theta_X \quad (55)$$

$$E(t) = D_T \Delta T(t) + D_{\dot{T}} \dot{T}(t) + \bar{D}_{GRAD\dot{T}} \bullet GRAD\dot{T}(t) \quad (56)$$

$$D(t) = D_F + D_{RN} + D_{RB} + D_{RK} + D_{RR} + D_Q \quad (57)$$

$$\varepsilon_k(t) = \varepsilon_T \Delta T(t) + f(\omega(t)) \quad (58)$$

where

- $\omega_{IRA}(t), \omega_{XRA}(t), \omega_{YRA}(t)$ = applied angular velocities about the IRA, XRA, and YRA axes, respectively, deg/s
- θ_X, θ_Y = misalignment of the IA axis about the XRA and YRA axes, respectively, deg
- D_T = drift rate temperature sensitivity coefficient, deg/ $^{\circ}$ s
- $D_{\dot{T}}$ = temperature ramp drift rate sensitivity coefficient, deg/ $^{\circ}$
- $\bar{D}_{GRAD\dot{T}}$ = coefficient vector of time-varying temperature gradient drift rate sensitivity vector, deg-cm/ $^{\circ}$
- $\Delta T(t)$ = temperature change, $^{\circ}$
- $\dot{T}(t)$ = temperature time-rate-of-change, %/s
- $GRAD\dot{T}(t)$ = gradient of the temperature, $^{\circ}$ /cm
- D_F = bias, arcsec/s
- D_{RN} = random drift rate due to angle random walk, deg/s
- D_{RB} = random drift rate due to bias instability, deg/s
- D_{RK} = random drift rate due to rate random walk, deg/s
- D_{RR} = random drift rate due to rate ramp, deg/s

D_Q = combined effect of apparent equivalent random drift rate due to angle quantization, and the apparent equivalent random drift rate due to the anti-lock residual, random drift rate from angle random walk, deg/s

ε_T = scale factor temperature sensitivity coefficient, ppm/ $^{\circ}$ C
 $f(\omega(t))$ = scale factor errors dependent on input rate, ppm

Substitution of Equations (54)-(58) into Equation (53) yields

$$K_0 f(t) = [\omega_{IR4}(t) + \omega_{XRA}(t) \sin \theta_Y - \omega_{YRA}(t) \sin \theta_X \\ + D_T \Delta T(t) + D_{\dot{T}} \dot{T}(t) + \bar{D}_{GRAD\dot{T}} \bullet GRAD\dot{T}(t) + D_F + D_{RN} \\ + D_{RB} + D_{RK} + D_{RR} + D_Q] / [1 + 10^{-6} \varepsilon_T \Delta T(t) + f(\omega(t))] + \varepsilon(t) \quad (59)$$

Taking the Laplace Transform of Equation (59) gives the model equation in the s-plane in terms of the applied angular velocities and model coefficients, from which a SIMULINK block diagram can be constructed, as

$$K_0 f(s) = [\omega_{IR4}(s) + \omega_{XRA}(s) \sin \theta_Y - \omega_{YRA}(s) \sin \theta_X \\ + D_T \Delta T(s) + D_{\dot{T}} \dot{T}(s) + \bar{D}_{GRAD\dot{T}} \bullet GRAD\dot{T}(s) + D_F + D_{RN} \\ + D_{RB} + D_{RK} + D_{RR} + D_Q] / [1 + 10^{-6} \varepsilon_T \Delta T(s) + f(\omega(s))] \quad (60)$$

The right side of Equation (60) again represents the sensed rotation rate of the gyro, and integration of the right side will provide the angular position using the relationship

$$s \theta_o(s) = \omega(s) \quad (61)$$

Further, the solution of Equation (60) for $f(s)$ will yield the pulse rate of the gyro. Both can be done within the block diagram model.

IEEE (1998) also recommends a simple closed-loop block diagram in the development of Equation (53). Application of the same block diagram for use with Equation (60) produces the complete mathematical model for an IFOG. This model is provided in Figure 20 below. Using the block diagram to solve for the angular position gives

$$\theta_0(s) = [\omega_{IR4}(s) + \omega_{XRA}(s) \sin \theta_Y - \omega_{YRA}(s) \sin \theta_X \\ + D_T \Delta T(s) + D_{\dot{T}} \dot{T}(s) + \bar{D}_{GRAD\dot{T}} \bullet GRAD\dot{T}(s) + D_F + D_{RN} \\ + D_{RB} + D_{RK} + D_{RR} + D_Q] / s[1 + 10^{-6} \varepsilon_T \Delta T(s) + f(\omega(s))] \quad (62)$$

For IFOGs, manufacturer's specification sheets often provide information scale factor, nonlinearity, bias, and angle random walk which could be used directly in the model. The other model coefficients must be obtained through testing procedures.

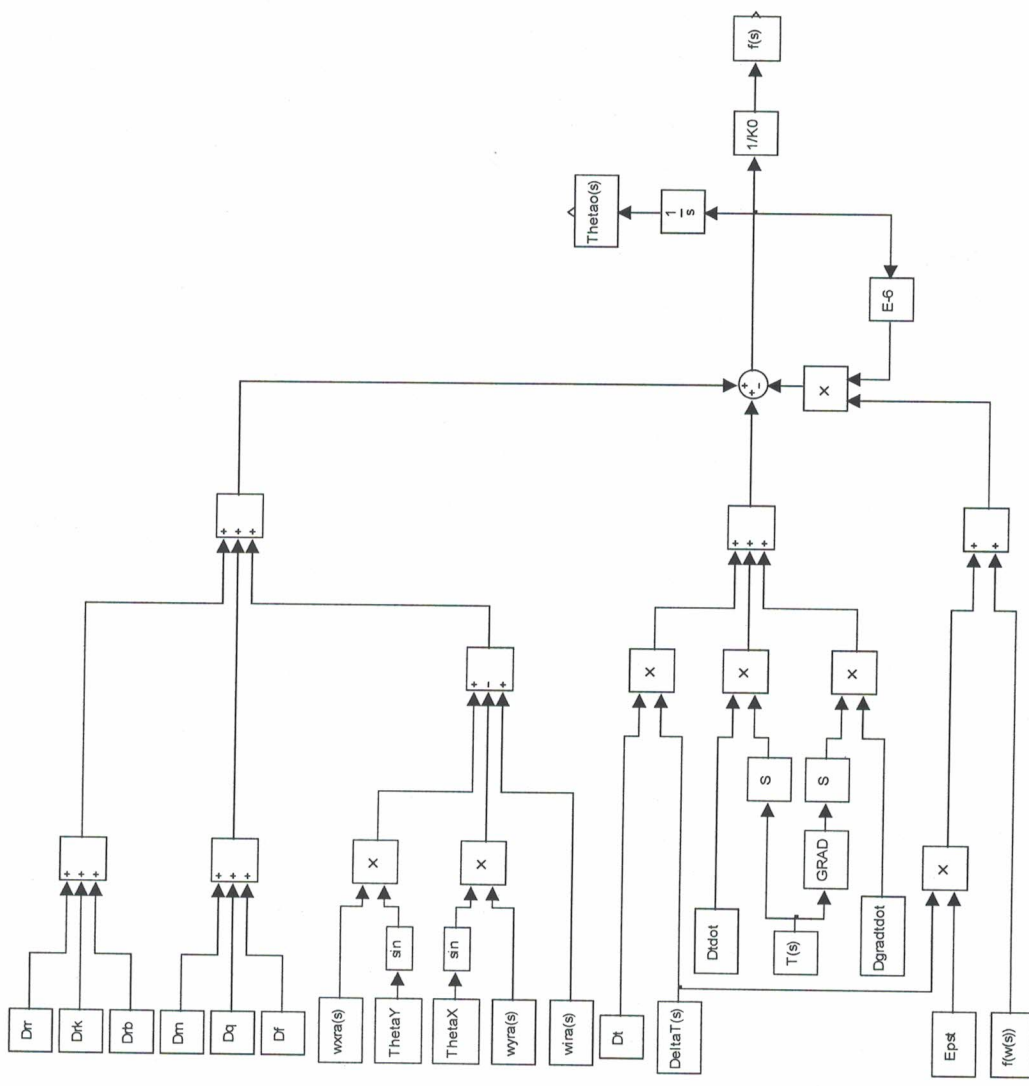


Figure 20. Interferometric Fiber Optic Gyro Closed-Loop Block Diagram

5.5 Coriolis Vibratory Gyro

A CVG is based on the coupling of a structural, driven, vibrating mode into at least one other structural, i.e., pickoff, mode via Coriolis acceleration, where the Coriolis force arises from the motion of the vibrating structure relative to the gyro case that is rotating relative to inertial space. Types of commercial available CVGs include: prismatic and triangular vibrating beams; single, dual, and multi-tine tuning forks; hemispherical, ring, and cylindrical vibrating shells; and, linear disk, angular disk, and linear plate vibrating plates. These CVGs all represent single degree-of-freedom devices.

IEEE (2004) provides the standards specification and test procedures for CVGs. The recommended model equation is nearly identical to the model equations previously presented for both ring laser gyros and IFOGs, however additional error terms are included. This standard does, however, present slightly different models for different CVG output types. These output types include: analog, digital, frequency, ratiometric, and whole angle mode outputs. Although these various models differ only slightly, the model for digital output will be presented here.

The model equation for a single-axis CVG expresses the relationship between the input rotation rate and the gyro output in terms of parameters whose coefficients are necessary to specify the performance of the CVG. The coordinate system used for this model is shown in Figure 21, along with the axis misalignment angles.

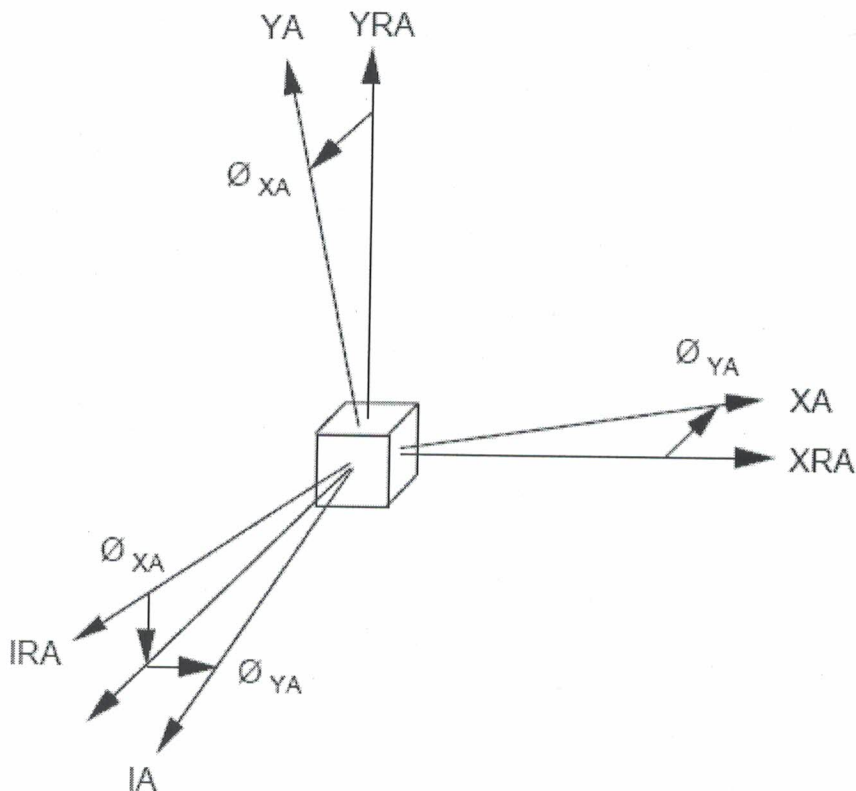


Figure 21. Coriolis Vibratory Gyro Coordinate System and Misalignment Angles

The model equation for digital output is presented as

$$K_0 V_d(t) = [\omega(t) + E(t) + D(t)]/[1 + 10^{-6} \varepsilon_k(t)] + \varepsilon(t) \quad (63)$$

where

- K_0 = gyro scale factor, (deg/h)/LSB
- $V_d(t)$ = digital output, LSBs
- $\omega(t)$ = sensed angular velocity of gyro case, deg/h
- $E(t)$ = environmentally sensitive drift rate, deg/h
- $D(t)$ = drift rate, deg/h
- $\varepsilon_k(t)$ = scale factor error, ppm
- $\varepsilon(t)$ = random measurement and process noise, deg/h
- LSB = least significant bit of the digital word representing the angle change

The individual terms in Equation (63) are further defined as

$$\omega(t) = \omega_{IRA}(t) + \omega_{XRA}(t) \sin \theta_Y - \omega_{YRA}(t) \sin \theta_X \quad (64)$$

$$\begin{aligned} E(t) = & D_T \Delta T(t) + D_{\dot{T}} \dot{T}(t) + \bar{D}_{GRADT} \bullet GRADT(t) + D_c a_{VR} \\ & + D_{\Delta F} a_{V\Delta F} + D_D a_{VD} + D_P a_{VP} + D_{SR} a_{VSR} + D_a a \\ & + D_{RI} a_{VOF} (\omega_{XRA} + \omega_{YRA}) + D_{RBB} a_{VBB} \end{aligned} \quad (65)$$

$$D(t) = D_F + D_{RN} + D_{RB} + D_{RK} + D_{RR} + D_{RM} + D_{RQ} \quad (66)$$

$$\varepsilon_k(t) = \varepsilon_{KO} + \varepsilon_T \Delta T(t) + S_a a \quad (67)$$

where

- $\omega_{IRA}(t), \omega_{XRA}(t), \omega_{YRA}(t)$ = applied angular velocities about the IRA, XRA, and YRA axes, respectively, deg/h
- θ_X, θ_Y = misalignment of the IA axis about the XRA and YRA axes, respectively, deg
- D_T = drift rate temperature sensitivity coefficient, deg/h-°
- $D_{\dot{T}}$ = temperature ramp drift rate sensitivity coefficient, deg/°/s
- \bar{D}_{GRADT} = coefficient vector of time-varying temperature gradient drift rate sensitivity vector, deg-cm/°-s
- $\Delta T(t)$ = temperature change, °
- $\dot{T}(t)$ = temperature time-rate-of-change, °/s
- $GRADT(t)$ = gradient of the temperature, °/cm
- D_c = drift rate vibration induced coning sensitivity coefficient, deg/h-g
- $D_{\Delta F}$ = drift rate sensitivity coefficient due to random vibration around the difference frequency, $a_{V\Delta F}$, deg/h-g
- D_D = drift rate sensitivity coefficient due to random vibration input around the difference frequency, deg/h-g

D_P = drift rate sensitivity coefficient due to random vibration input around pickoff frequency, deg/h-g
 D_{SR} = drift rate structural resonance sensitivity coefficient due to random vibration input around a structural resonance, deg/h-g
 D_a = drift rate acceleration sensitivity coefficient due to acceleration a along that axis, deg/h-g
 D_{RI} = drift cross-axis vibration sensitivity coefficient due to random vibration around the operating frequency and a constant input rate about an axis orthogonal to the input axis.
 D_{RBB} = noise sensitivity coefficient due to broadband input vibration coupled with pickoff asymmetry, deg/h-g
 D_F = bias, deg/h
 D_{RN} = random drift rate due to angle random walk, deg/h
 D_{RB} = random drift rate due to bias instability, deg/h
 D_{RK} = random drift rate due to rate random walk, deg/h
 D_{RR} = random drift rate due to rate ramp, deg/h
 D_{RM} = random drift rate due to Markov noise, deg/h
 D_{RQ} = drift rate due to output quantization, deg/h
 ε_{KO} = scale factor error at nominal conditions, ppm
 ε_T = scale factor temperature sensitivity coefficient, ppm/ $^{\circ}$
 S_a = scale factor acceleration sensitivity coefficient due to acceleration a along that axis, ppm/g
 $avr(t)$ = random vibration acceleration around resonance, g
 $av_{\Delta F}(t)$ = random vibration acceleration around the difference frequency, g
 $av_D(t)$ = random vibration acceleration around the drive frequency, g
 $av_P(t)$ = random vibration acceleration around the pickoff frequency, g
 $av_{SR}(t)$ = random vibration acceleration around a structural resonance, g
 $a(t)$ = acceleration applied along any given axis, g
 $av_{OF}(t)$ = random vibration acceleration around the operating frequency, g
 $av_{BB}(t)$ = broadband vibration acceleration, g

Substitution of Equations (64)-(67) into Equation (63) yields

$$\begin{aligned}
 K_0 V_d(t) = & [\omega_{IRA}(t) + \omega_{XRA}(t) \sin \theta_Y - \omega_{YRA}(t) \sin \theta_X \\
 & + D_T \Delta T(t) + D_{\dot{T}} \dot{T}(t) + \bar{D}_{GRADT} \bullet GRADT(t) + D_c a_{VR}(t) \\
 & + D_{\Delta F} a_{V\Delta F}(t) + D_D a_{VD}(t) + D_P a_{VP}(t) + D_{SR} a_{VSR}(t) + D_a a(t) \\
 & + D_{RI} a_{VOF}(t)(\omega_{XRA}(t) + \omega_{YRA}(t)) + D_{RBB} a_{VBB}(t) + D_F + D_{RN} \\
 & + D_{RB} + D_{RK} + D_{RR} + D_{RM} + D_{RQ}] \\
 & /[1 + 10^{-6}(\varepsilon_{KO} + \varepsilon_T \Delta T(t) + S_a a(t))] + \varepsilon(t)
 \end{aligned} \tag{68}$$

Taking the Laplace Transform of Equation (68) gives the model equation in the s-plane in terms of the applied angular velocities and model coefficients, from which a SIMULINK block diagram can be constructed, as

$$\begin{aligned}
K_0 V_d(s) = & [\omega_{IR_A}(s) + \omega_{XR_A}(s) \sin \theta_Y - \omega_{YR_A}(s) \sin \theta_X \\
& + D_T \Delta T(s) + D_{\dot{T}} \dot{T}(s) + \bar{D}_{GRADT} \bullet GRADT(s) + D_c a_{VR}(s) \\
& + D_{\Delta F} a_{V\Delta F}(s) + D_D a_{VD}(s) + D_P a_{VP}(s) + D_{SR} a_{VSR}(s) \\
& + D_a a(s) + D_{RI} a_{VOF}(s)(\omega_{XR_A}(s) + \omega_{YR_A}(s)) + D_{RBB} a_{VBB}(s) \\
& + D_F + D_{RN} + D_{RB} + D_{RK} + D_{RR} + D_{RM} + D_{RQ}] \\
& / [1 + 10^{-6} (\varepsilon_{KO} + \varepsilon_T \Delta T(s) + S_a a(s))]
\end{aligned} \tag{69}$$

The right side of Equation (69) again represents the sensed rotation rate of the gyro, and integration of the right side will provide the angular position using the relationship

$$s \theta_o(s) = \omega(s) \tag{70}$$

Further, the solution of Equation (69) for $V_d(s)$ will yield the digital output of the gyro. Both can be done within the block diagram model.

The same simple closed-loop block diagram used for the ring laser gyro and IFOG is recommended by IEEE (2004) for the CVG. Application of that block diagram with Equation (70) produces the complete mathematical model for a CVG. This model is provided in Figure 22 below. Using the block diagram to solve for the angular position gives

$$\begin{aligned}
\theta_o(s) = & [\omega_{IR_A}(s) + \omega_{XR_A}(s) \sin \theta_Y - \omega_{YR_A}(s) \sin \theta_X \\
& + D_T \Delta T(s) + D_{\dot{T}} \dot{T}(s) + \bar{D}_{GRADT} \bullet GRADT(s) + D_c a_{VR}(s) \\
& + D_{\Delta F} a_{V\Delta F}(s) + D_D a_{VD}(s) + D_P a_{VP}(s) + D_{SR} a_{VSR}(s) \\
& + D_a a(s) + D_{RI} a_{VOF}(s)(\omega_{XR_A}(s) + \omega_{YR_A}(s)) + D_{RBB} a_{VBB}(s) \\
& + D_F + D_{RN} + D_{RB} + D_{RK} + D_{RR} + D_{RM} + D_{RQ}] \\
& / s [1 + 10^{-6} (\varepsilon_{KO} + \varepsilon_T \Delta T(s) + S_a a(s))]
\end{aligned} \tag{71}$$

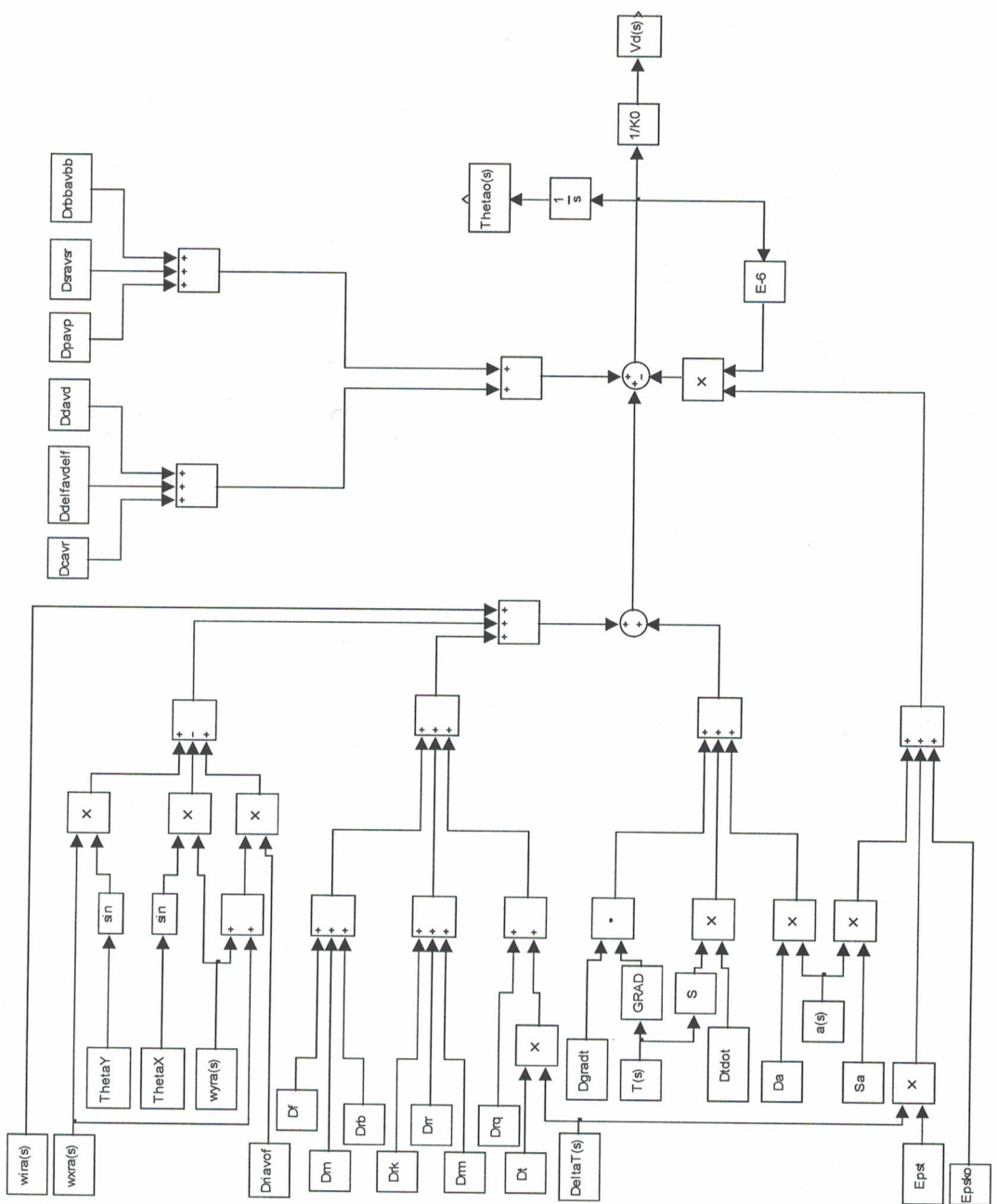


Figure 22. Coriolis Vibratory Gyro Closed-Loop Block Diagram

5.6 Dynamically Tuned Gyro

A dynamically tuned gyro (DTG) differs from the gyros previously discussed in this report in that a DTG has two degrees-of-freedom rather than a single degree-of-freedom. The complexity of the model is significantly increased as a result of this second degree-of-freedom. The derivation of comprehensive mathematical models for DTG are presented by Craig (1972(a), 1972(b), and 1990), and Junqueira and de Barros (2004). These models are summarized by IEEE (1989) and will be presented here in the form of a practical mathematical model of a DTG.

A mechanical schematic of a DTG, along with the axes misalignment angles, α , β , γ_x , and γ_y , was also presented in IEEE (1989) and is provided here as Figure 23. This diagram shows the two degrees-of-freedom of a DTG to be angular rotations about the X and Y axes. The angular rotations about these axes are balanced by command rate torquer currents. The sign conventions for the DTG indicate that a positive current applied to the X torquer will balance a positive input rate about the Y axis; and a positive current applied to the Y torquer will balance a negative input rate about the X axis.

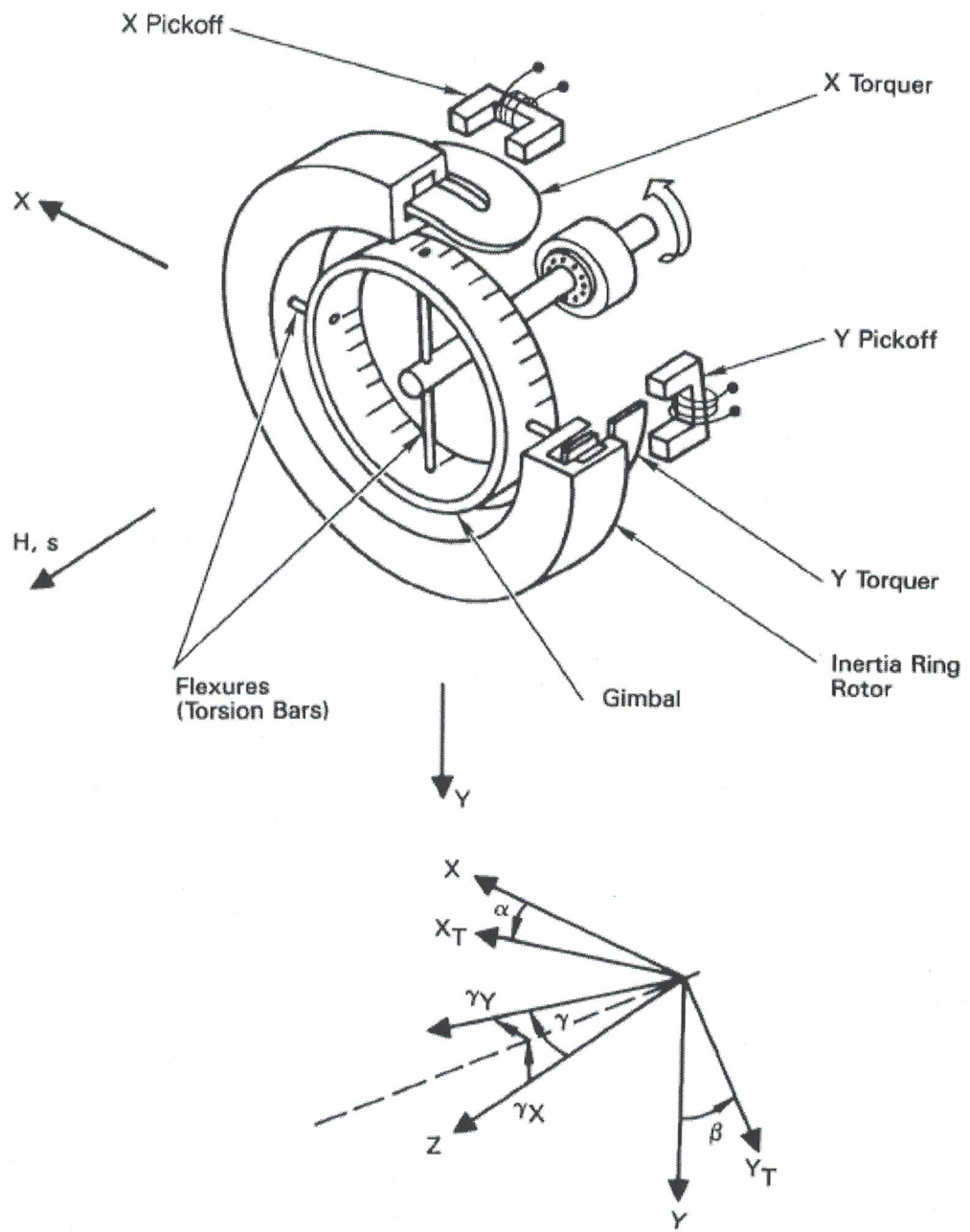


Figure 23. Dynamically Tuned Gyro Mechanical Schematic and Misalignment Angles

The two resulting coupled equations of motion of the DTG are developed to relate the angular motions of the case and inertial acceleration inputs to the command rate torquer currents. These dynamical equations for rotation about the gyro x and y axes can be written as

$$\begin{aligned} I_x \ddot{\theta}_x(t) + H \dot{\theta}_y(t) - H_g \dot{\theta}_Y(t) - f(\dot{\theta}_x(t) - \dot{\theta}_x(t)) \\ - K_D(\theta_x(t) - \theta_x(t)) - K_Q(\theta_Y(t) - \theta_y(t)) = HM_x(t) \end{aligned} \quad (72)$$

$$\begin{aligned} I_y \ddot{\theta}_y(t) - H \dot{\theta}_x(t) + H_g \dot{\theta}_X(t) - f(\dot{\theta}_Y(t) - \dot{\theta}_y(t)) \\ - K_D(\theta_Y(t) - \theta_y(t)) + K_Q(\theta_X(t) - \theta_x(t)) = HM_y(t) \end{aligned} \quad (73)$$

where

$\theta_x(t), \theta_y(t)$ = angular displacements of the rotor about the x and y axes,
respectively, with respect to inertial space, rad

$\dot{\theta}_x(t), \dot{\theta}_y(t)$ = angular velocities of the rotor about the x and y axes,
respectively, with respect to inertial space, rad/s

$\ddot{\theta}_x(t), \ddot{\theta}_y(t)$ = angular accelerations of the rotor about the x and y axes,
respectively, with respect to inertial space, rad/s²

$\theta_X(t), \theta_Y(t)$ = angular displacements of the case about the X and Y axes,
respectively, with respect to inertial space, rad

I_x, I_y = mass moments of inertia of the rotor about the x and y axes,
respectively, g-cm²

H = angular momentum of the rotor, g-cm²/s

H_g = effective angular momentum of the gimbal, g-cm²/s

f = damping coefficient of the rotor, g-cm²/s

K_D = direct spring constant, dyn-cm

K_Q = quadrature spring rate, dyn-cm

$M_x(t), M_y(t)$ = applied rotations about the x and y axes, respectively, rad/s

Taking the Laplace Transforms of Equations (72) and (73) allows them to be written in the s-plane as

$$\begin{aligned} I_x s^2 \theta_x(s) + H s \theta_y(s) - H_g s \theta_Y(s) - f(s \theta_x(s) - \theta_x(s)) \\ - K_D(\theta_x(s) - \theta_x(s)) - K_Q(\theta_Y(s) - \theta_y(s)) = HM_x(s) \end{aligned} \quad (74)$$

$$\begin{aligned} I_y s^2 \theta_y(s) - H s \theta_x(s) + H_g s \theta_X(s) - f(s \theta_Y(s) - s \theta_y(s)) \\ - K_D(\theta_Y(s) - \theta_y(s)) + K_Q(\theta_X(s) - \theta_x(s)) = HM_y(s) \end{aligned} \quad (75)$$

where

s = Laplace operator

$\theta_x(s), \theta_y(s)$ = Laplace Transform of the angular displacements of the
rotor about the x and y axes, $\theta_x(t), \theta_y(t)$, respectively, with respect
to inertial space, rad

$\theta_X(s), \theta_Y(s)$ = Laplace Transform of the angular displacements of the
case about the X and Y axes, $\theta_X(t), \theta_Y(t)$, respectively, with
respect to inertial space, rad

$M_x(s), M_y(s)$ = Laplace Transform of the applied rotations about the x and axes, $M_x(t), M_y(t)$, respectively, rad/s

Solving Equations (74) and (75) for the rotation angle outputs, $\theta_x(s)$ and $\theta_y(s)$, in terms of the applied rotations, $M_x(s)$ and $M_y(s)$ gives

$$\begin{aligned}\theta_y(s) &= [HM_x(s) - (I_x s^2 + fs + K_D) \theta_x(s) + \\ &(fs + K_D) \theta_x(s) + (K_Q + H_g s) \theta_y(s)] / (Hs + K_Q)\end{aligned}\quad (76)$$

$$\begin{aligned}\theta_x(s) &= [HM_y(s) - (I_y s^2 + fs + K_D) \theta_y(s) + \\ &(fs + K_D) \theta_y(s) - (K_Q + H_g s) \theta_x(s)] / (-Hs - K_Q)\end{aligned}\quad (77)$$

Since Equations (76) and (77) are coupled and create a natural feedback scenario, together they represent the closed-loop transfer functions for a DTG. The corresponding block diagram is shown in Figure 24.

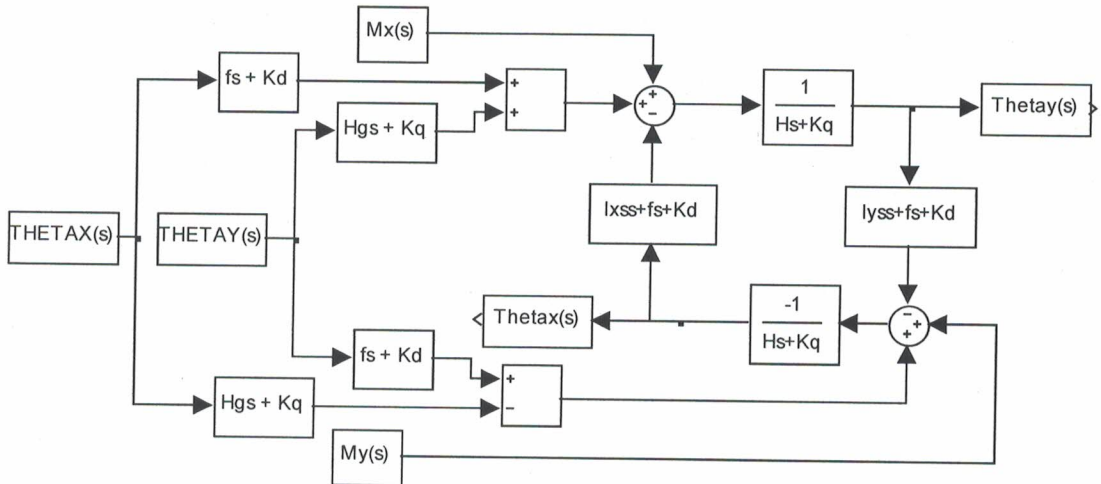


Figure 24. Dynamically Tuned Gyro Closed-Loop Block Diagram (Dynamics-Only)

The applied rotations, $M_x(t)$ and $M_y(t)$, can each be separated into two components representing the sum of the actual rotations, $M_x^c(t)$ and $M_y^c(t)$, and the rotation errors, $M_x^e(t)$ and $M_y^e(t)$, as

$$M_x(t) = M_x^c(t) + M_x^e(t) \quad (78)$$

$$M_y(t) = M_y^c(t) + M_y^e(t) \quad (79)$$

and

$$M_x^e(t) = K_{TX} i_X(t) \quad (80)$$

$$M_y^e(t) = K_{TY} i_Y(t) \quad (81)$$

where

K_{TX}, K_{TY} = composite command rate scale factors in the X and Y directions, respectively, rad/s-A

$i_X(t), i_Y(t)$ = torque current in the X and Y directions, respectively, A

IEEE (1989) provides expressions for the rotation errors which consist of a series of terms that mathematically relate the outputs of the DTG to several acceleration and rate inputs. These rotation errors can be written as

$$\begin{aligned} M_x^e(t) &= \omega_Y(t) + \beta\omega_X(t) + \gamma_X\omega_Z(t) + D(y)_F + D(y)_X a_X(t) \\ &+ D(y)_Y a_Y(t) + D(y)_Z a_Z(t) + D(y)_{XZ} a_X(t) a_Z(t) \\ &+ D(y)_{YZ} a_Y(t) a_Z(t) + [(J - I)/H]\omega_Y(t)\omega_Z(t) + \theta_X(t)\omega_Z(t) + \varepsilon_X(t) \end{aligned} \quad (82)$$

$$\begin{aligned} M_y^e(t) &= \omega_X(t) + \alpha\omega_Y(t) - \gamma_Y\omega_Z(t) + D(x)_F + D(x)_X a_X(t) \\ &+ D(x)_Y a_Y(t) + D(x)_Z a_Z(t) + D(x)_{XZ} a_X(t) a_Z(t) \\ &+ D(x)_{YZ} a_Y(t) a_Z(t) + [(J - I)/H]\omega_X(t)\omega_Z(t) - \theta_Y(t)\omega_Z(t) + \varepsilon_Y(t) \end{aligned} \quad (83)$$

where

$\omega_X(t), \omega_Y(t), \omega_Z(t)$ = applied angular velocities of the gyro case about the X, Y, and Z axes, respectively, rad/s

$a_X(t), a_Y(t), a_Z(t)$ = linear accelerations along the X, Y, and Z axes, respectively, g

β = misalignment of the Y torquer axis, Y_T , about the Z axis with respect to the Y axis of the case, rad

α = misalignment of the X torquer axis, X_T , about the Z axis with respect to the X axis of the case, rad

γ_X = misalignment of the rotor spin axis about the X axis of the case with respect to the Z axis, rad

γ_Y = misalignment of the rotor spin axis about the Y axis of the case with respect to the Z axis, rad

$D(y)_F, D(x)_F$ = bias drift rate coefficients, rad/s

$D(y)_X, D(y)_Y, D(y)_Z, D(x)_X, D(x)_Y, D(x)_Z$ = acceleration-sensitive drift rate coefficients, rad/s-g

$D(y)_{XZ}, D(y)_{YZ}, D(x)_{XZ}, D(y)_{YZ}$ = second order acceleration-sensitive drift rate coefficients, rad/s-g²

J = effective rotor mass moment of inertia, g-cm²

I = effective rotor transverse moment of inertia, g-cm²

H = angular momentum of the rotor, g-cm²/s

$\varepsilon(t)$ = random measurement and process noise, rad/s

In Equations (82) and (83) above, the cross-coupling drift rate error terms, $\theta_x \omega_z$ and $-\theta_y \omega_z$, and the anisoinertial drift rate error terms, $[(J-I)/H]\omega_Y\omega_Z$ and $[(J-I)/H]\omega_X\omega_Z$, are typically very small and could be neglected without a significant loss of accuracy in the model.

Again, the bias and axis misalignment modeling coefficients can often be obtained from the manufacturer's specification sheets for commercially available gyros. The values of the other coefficients are generally not available from the manufacturer and must be obtained through testing and calibration of each unit. Additional information regarding the mathematical form, physical meaning, and procedures for accelerometer testing and mathematical form, physical meaning, and procedures for accelerometer testing and calibration is provided by the IEEE (1989). Upon performing the specified tests, the method of least squares can be used to determine the values of the model coefficients using the data obtained in the testing program.

Substitution of Equations (80)-(83) into Equations (78) and (79) gives the results

$$\begin{aligned} M_x(t) = & K_{TX} i_X(t) + \omega_Y(t) + \beta \omega_X(t) + \gamma_X \omega_Z(t) + D(y)_F \\ & + D(y)_X a_X(t) + D(y)_Y a_Y(t) + D(y)_Z a_Z(t) + D(y)_{XZ} a_X(t) a_Z(t) \quad (84) \\ & + D(y)_{YZ} a_Y(t) a_Z(t) + [(J-I)/H] \omega_Y(t) \omega_Z(t) + \theta_x(t) \omega_Z(t) + \varepsilon_x(t) \end{aligned}$$

$$\begin{aligned} M_y(t) = & K_{TY} i_Y(t) + \omega_X(t) + \alpha \omega_Y(t) - \gamma_Y \omega_Z(t) + D(x)_F \\ & + D(x)_X a_X(t) + D(x)_Y a_Y(t) + D(x)_Z a_Z(t) + D(x)_{XZ} a_X(t) a_Z(t) \quad (85) \\ & + D(x)_{YZ} a_Y(t) a_Z(t) + [(J-I)/H] \omega_X(t) \omega_Z(t) - \theta_y(t) \omega_Z(t) + \varepsilon_y(t) \end{aligned}$$

In addition, the random measurement and process noise can again be modeled in a guidance system Kalman filter model using augmented Markov process states and will not appear in the model equation upon taking the Laplace Transform of Equations (84) and (85). Taking these Laplace Transforms gives

$$\begin{aligned} M_x(s) = & K_{TY} i_Y(s) + \omega_Y(s) + \beta \omega_X(s) + \gamma_X \omega_Z(s) + D(y)_F \\ & + D(y)_X a_X(s) + D(y)_Y a_Y(s) + D(y)_Z a_Z(s) + D(y)_{XZ} a_X(s) a_Z(s) \quad (86) \\ & + D(y)_{YZ} a_Y(s) a_Z(s) + [(J-I)/H] \omega_Y(s) \omega_Z(s) + \theta_x(s) \omega_Z(s) \end{aligned}$$

$$\begin{aligned} M_y(s) = & K_{TY} i_Y(s) + \omega_X(s) + \alpha \omega_Y(s) - \gamma_Y \omega_Z(s) + D(x)_F \\ & + D(x)_X a_X(s) + D(x)_Y a_Y(s) + D(x)_Z a_Z(s) + D(x)_{XZ} a_X(s) a_Z(s) \quad (87) \\ & + D(x)_{YZ} a_Y(s) a_Z(s) + [(J-I)/H] \omega_X(s) \omega_Z(s) - \theta_y(s) \omega_Z(s) \end{aligned}$$

Substitution of Equations (86) and (87) into Equations (76) and (77) gives the solution for the angular position output for the two degree-of-freedom DTG as

$$\begin{aligned}
\theta_y(s) = & \{H[K_{TY}i_Y(s) + \omega_Y(s) + \beta\omega_X(s) + \gamma_X\omega_Z(s) + D(y)_F \\
& + D(y)_X a_X(s) + D(y)_Y a_Y(s) + D(y)_Z a_Z(s) + D(y)_{XZ} a_X(s)a_Z(s) \\
& + D(y)_{YZ} a_Y(s)a_Z(s) + [(J-I)/H]\omega_Y(s)\omega_Z(s) + \theta_x(s)\omega_Z(s)] \\
& - (I_x s^2 + fs + K_D)\theta_x(s) + (fs + K_D)\theta_X(s) \\
& + (K_Q + H_g s)\theta_Y(s)\} / (Hs + K_Q)
\end{aligned} \quad (88)$$

$$\begin{aligned}
\theta_x(s) = & \{H[K_{TY}i_Y(s) + \omega_X(s) + \alpha\omega_Y(s) - \gamma_Y\omega_Z(s) + D(x)_F \\
& + D(x)_X a_X(s) + D(x)_Y a_Y(s) + D(x)_Z a_Z(s) + D(x)_{XZ} a_X(s)a_Z(s) \\
& + D(x)_{YZ} a_Y(s)a_Z(s) + [(J-I)/H]\omega_X(s)\omega_Z(s) - \theta_y(s)\omega_Z(s)] \\
& - (I_y s^2 + fs + K_D)\theta_y(s) + (fs + K_D)\theta_Y(s) \\
& - (K_Q + H_g s)\theta_X(s)\} / (-Hs - K_Q)
\end{aligned} \quad (89)$$

This representation will be used in the development of a SIMULINK block diagram for the complete DVG model combining the dynamical model and the error terms. This SIMULINK model is given in Figure 25. This model can also be converted to a complete, working SIMULINK model without a major program effort.

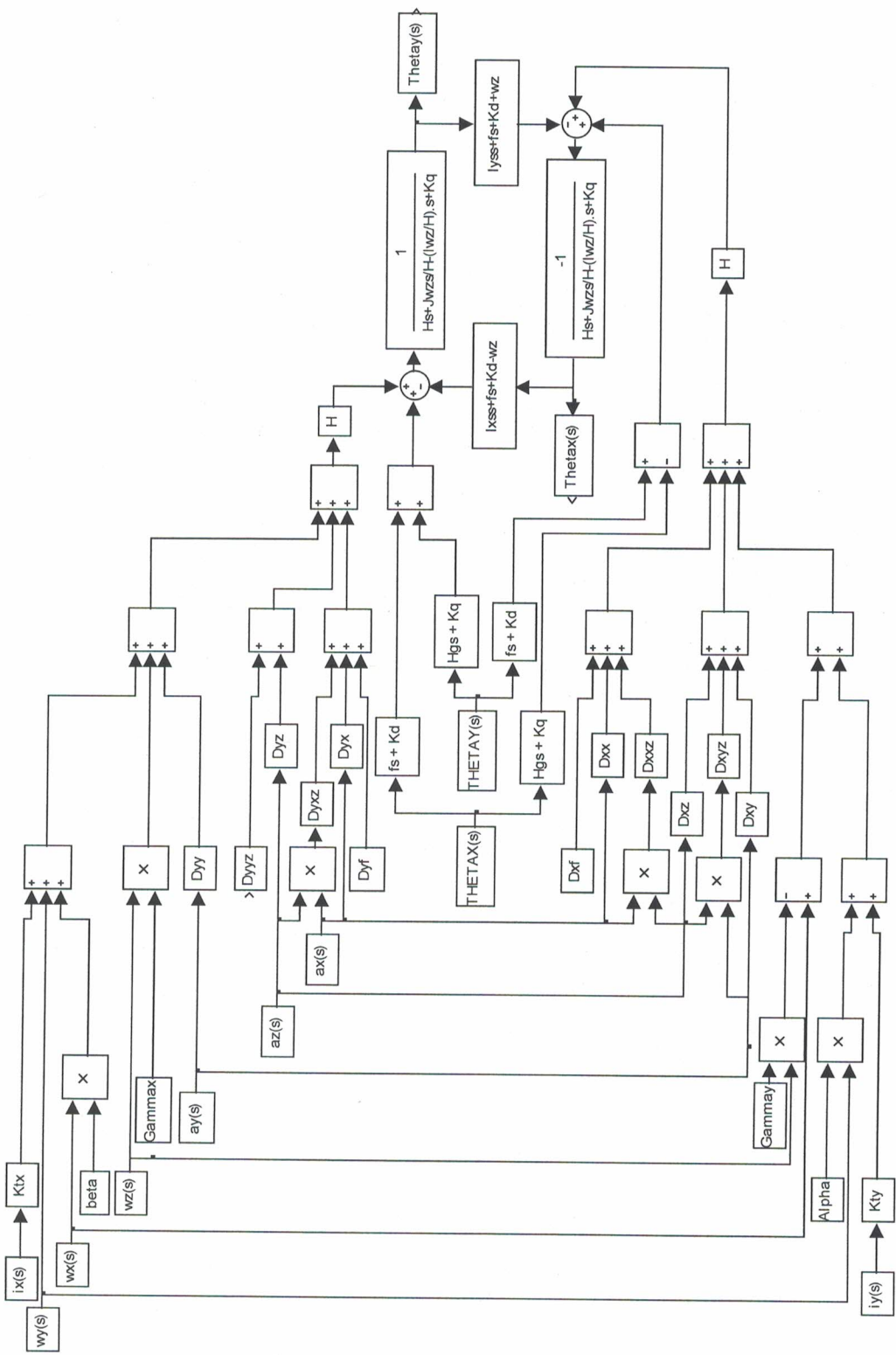


Figure 25. Dynamically Tuned Gyro Closed-Loop Block Diagram

6.0 Allan Variance Techniques

As stated earlier in this report, the random measurement and process noise which appears in the error models, could have quantization, white, random walk, flicker, or other components. The process noise distinct from the noise due to the analog-to-digital converter, voltage-to-frequency converter, or other digitization readout system can be regarded as accelerometer random bias instability, separate from any systematic models of bias variation such as trend or temperature and other sensitivities. This random noise component must be modeled using a Kalman filter.

The characterization of the random measurement and process noise can be performed using Allan variance techniques. The Allan variance analysis method models the inertial sensor random noise and the sources of this noise can be then be identified (and modeled) for overall model improvement. If the noise model is accurate, the navigation performance of the IMU will be improved. Kim, et al (2004) use Allan variance techniques to improve the performance of a GPS/INS system model, and Flenniken and Hamm (2004) use Allan variance techniques to verify bias errors in accelerometers and rate gyros when combined with GPS tracking data. Hou (2004) also provides an in-depth discussion of the use of Allan variance in the modeling of inertial sensor errors. Many of the cited IEEE documents referenced in this report also discuss the implementation of the Allan variance method in the analysis of both accelerometer and gyro performance and modeling.

The Allan variance method was initially developed by David Allan of the National Bureau of Standards to quantify the error statistics of a Cesium beam frequency standard, but can be used to analyze the noise characteristics of any precision measurement instrument. A general discussion of the Allan variance method and its background, theory, and capabilities is provided by David Allan at the website: <http://www.allanstime.com/AllanVariance/index.html>. The major advantage of the Allan variance method is that it allows for a finer, easier characterization and identification of noise sources and the contribution to the overall noise statistics.

The mathematical theory behind the Allan variance method is not presented in this report, but a summary of the mathematical concepts and an outline of the algorithm are provided by Keim, et al (2004). As stated in that report, “the most attractive feature of Allan variance is its ability to sort out various noise components by the slopes of the root Allan variance plot provided the different noise mechanisms are reasonably separated in the frequency and time domain.” Many different random noise components may be present in sensor data, depending on the sensor type and the environment in which the data are obtained. The relationship between the Allan variance and the noise source characterization can then be determined and the various random noise sources can be modeled. If the noise sources are statistically independent, the computed Allan variance will be equal to the sum of the squares of each noise type and the level of contribution for each component can be extracted using the method of least squares. The results can then be used to improve the modeling of the random measurement and process noise in both accelerometers and gyros.

In the development of high fidelity mathematical models for accelerometers and gyros, use of the Allan variance method should be considered in order to better model the random noise components which can greatly affect performance of those sensors.

7.0 Summary and Conclusions

This project has addressed the development of high fidelity mathematical models for IMUs for use as a future analysis tool. The intent of this modeling effort was to create mathematical models capable of being used to simulate the performance of both new and commercially available IMUs. It was found that the most effective approach to achieve this modeling goal was to develop separate mathematical models for the accelerometer and gyro sensors which comprise the IMUs. These individual sensor models can then be integrated in a complete IMU model in future development.

While a significant amount of literature was reviewed to examine mathematical modeling techniques currently being used for accelerometers and gyros, the most comprehensive collection of applicable literature was a series of standard specification and testing procedures published by the IEEE. These inertial sensors standards were developed by the Gyro and Accelerometer Panel of the IEEE Aerospace and Electronics Systems Society, and are published by the Standards Association of the IEEE. These documents provided a good starting point in the development of the desired models. Using the information available from those sources, it was possible to develop models which integrated the dynamical/physical and sensor error models into a system structure for inclusion with the stochastic and measurement models.

In this study high fidelity mathematical models were developed for the following specific IMU sensor components: translational proof-mass and pendulous/torque-balance accelerometers; and spring restrained rate, rate-integrating, ring laser, interferometric fiber optic, Coriolis vibratory, and dynamically tuned gyros. The models which were developed included the mathematical equations describing the dynamic/physical characteristics of the sensor, and mathematical expressions describing the many possible sources of measurement error which can occur in the sensors. The Allan variance technique was also discussed as a method to characterize the random components of measurement and process noise for accuracy improvement.

By combining the dynamical/physical and error models for each sensor, the overall system response can be achieved. From the system response, the associated time delays, response time, and system performance can be determined. This information will be very useful in the undertaking of design, analysis, and performance studies of the IMUs.

The high fidelity models of accelerometers and gyros developed in this study can be simplified by reducing the number of error terms if no information is available or can be determined about certain modeling parameters. The IEEE standard specifications and testing standards referenced in this report should be followed closely in the actual

implementation of the model and determination of the values of the modeling parameters. Many intricate details of the modeling and physical interpretation of the modeling coefficients are discussed in detail in those standards but could not be included in this study.

A most useful aspect in this development was the creation of block diagrams of the integrated model which can be subsequently extended to a full SIMULINK simulation for each sensor in order to create a fully-functioning dynamic simulation tool. These models can likely be achieved without a major development effort. A complete set of recommendations for future development are provided in the next section of this report.

It was originally hoped that the mathematical model which were developed would possess the capability to use data from manufacturer's product specifications to be able to closely mimic the performance of manufacturer's units. However, the information generally available from manufacturer's product specifications only provides data on a few of the error sources present in any particular unit. While this information can be used in the modeling of the unit, there are many other error terms represented in the modeling equations for the sensors for which no information is provided. Due to this lack of information, it is unlikely that accurate simulations of commercial units can be achieved solely with the information provided to the customer in the product specifications. In most cases it would appear that significant testing of a unit is necessary in order to determine a substantial set of error modeling parameters to be used in modeling the units. Without adequate testing it is unlikely that a highly accurate model of an IMU or its components can be developed. This conclusion is supported by Ang, et al (2004).

8.0 Recommendations for Future Development

In order to accomplish the goal of achieving a fully-functional IMU simulation tool, the following recommendations for future development need to be addressed:

1. Extension of the single-axis mathematical models of the accelerometers and gyros to the commonly-used three-axis, cluster models or use in IMUs.
2. Conversion of the single-axis block diagram representation of the system models to fully-functional, three-axis, cluster SIMULINK models.
3. Modeling of the random measurement and process noise at the Kalman filtering stage using the Allan variance (or similar) method to accurately model the random noise components which are present in each sensor.
4. Calibration and testing of the IMUs being modeled as prescribed by the IEEE Standard Specifications and Testing criteria in order to obtain the values of the many modeling parameter coefficients used in the high fidelity sensor models.

Upon completion of the recommended stated above, the capability will exist to simulate a variety of new and commercially available IMUs for use in design, analysis, and comparison studies of navigation systems and navigation system components. Since this capability does not currently exist, this development such a tool will represent a significant advance to existing technology.

9.0 Contact Information

I will continue to be available to discuss the contents of this Final Report, as well as the possibility of my future involvement in this and/or related projects. My permanent contact information is:

David A. Cicci, Ph.D., P.E.
Aerospace Engineering Department
211 Aerospace Engineering Building
Auburn University, AL 36849-5338
dcicci@eng.auburn.edu
334-844-6820
334-663-4579 (cell)
334-844-6803 (FAX)

I can also be contacted through:

Dynamic Concepts, Inc.
6700 Odyssey Drive, Suite 202
Huntsville, AL 35806
256-922-9850

or by contacting Dr. Tom Howsman at: thowsman@dynamic-concepts.com, or Mr. Philip Williams at: pwilliams@dynamic-concepts.com.

10.0 References

The references cited in this report are listed below. Copies of the supporting material which are provided on CD with this report are so indicated.

Ang, W. T., Khoo, S. Y., Khosla, P. K., and Riviere, C. N., "Physical Model of a MEMS Accelerometer for Low-g Motion Tracking Applications," Proceedings of the 2004 IEEE international Conference on Robotics & Automation, New Orleans, LA, April 2004. (Provided)

Aronowitz, F., "Fundamentals of the Ring Laser Gyro," Optical Gyros and Their Application, RTO AGARDograph 339, 1999.

Barbour, N., and Schmidt, G., "Inertial Technology Trends," IEEE Sensors Journal, Vol. 1, No. 4, pp. 332-339, December 2001. (Provided)

Brown, A., "GPS uses Low-Cost MEMS IMU," IEEE A&E Systems Magazine, pp. 3-10, September 2005. (Provided)

Chung, H., Ojeda, L., and Borenstein, J., "Accurate Mobile Robot Dead-reckoning With a Precision-Calibrated Fiber Optic Gyroscope," IEEE Transactions on Robotics and Automation, Vol. 17, No. 1, pp. 80-84, February 2001(a). (Provided)

Chung, H., Ojeda, L., and Borenstein, J., "Sensor Fusion for Mobile Robot Dead-reckoning With a Precision-calibrated Fiber Optic Gyroscope," IEEE International Conference on Robotics and Automation, pp. 3588-3593, May 2001(b). (Provided)

Craig, R., "Theory of Operation of an Elastically Supported, Tuned Gyroscope," IEEE Transactions on Aerospace and Electronic Systems, Vol. AES-8, No. 3, pp. 280-288, May 1972(a).

Craig, R., "Theory of Errors of a Multigimbal, Elastically Supported, Tuned Gyroscope," IEEE Transactions on Aerospace and Electronic Systems, Vol. AES-8, No. 3, pp. 289-297, May 1972(b).

Craig, R., "Theory of Operation of a Two-Axis-Rate Gyro," IEEE Transactions on Aerospace and Electronic Systems, Vol. 26, No. 5, pp. 722-731, September 1990. (Provided)

Curey, R., Ash, M., Thielman, L., and Barker, C., "Proposed IEEE Inertial Systems Terminology Standard and Other Inertial Sensor Standards," 2004 IEEE Position Location and Navigation Symposium (PLANS), pp. 83-90, April 2004. (Provided)

Dorobantu, R., and Gerlach, C., "Investigation of a Navigation-Grade RLG SIMU type iNAV-RQH," IAPG / FESG No. 16, Institut fur Astronomische und Physikalische Geodasie Forschungseinrichtung Satellitengeodasie, Technische Universitat Munchen, Munchen, Germany, 2004. (Provided)

Farrell, J. and Barth, M., *The Global Positioning System & Inertial Navigation*, McGraw-Hill Companies, Inc., New York, 1999.

Flenniken, W., and Hamm, C., "Final Report to Dan Lawrence, Phase IV Systems, Inc," Auburn University, Mechanical Engineering Department, GPS & Vehicle Dynamics Laboratory, March 26, 2004. (Provided)

Grewal, M., Weill, L., and Andrews, A., *Global Positioning Systems, Inertial Navigation, and Integration*, John Wiley & Sons, Inc., New York, 2001.

Hou, H., "Modeling Inertial Sensors Errors Using Allan Variance," UCGE Reports, Number 20201, University of Calgary, Department of Geomatics Engineering, September 2004. (<http://www.geomatics.ucalgary.ca/links/GradTheses.html>) (Provided)

IEEE Std. 292-1969, "IEEE Specification Format for Single-Degree-of-Freedom Spring-Restrained Rate Gyros," Institute of Electrical and Electronics Engineers, Inc., New York, 1969(a). (Provided)

IEEE Std. 293-1969, "IEEE Test Procedure for Single-Degree-of-Freedom Spring-Restrained Rate Gyros," Institute of Electrical and Electronics Engineers, Inc., New York, 1969(b). (Provided)

IEEE Std. 517-1974, "IEEE Standard Specification Format Guide and Test Procedure for Single Degree-of-Freedom Rate-Integrating Gyros," IEEE Aerospace and Electronic Systems Society, Gyro and Accelerometer Panel, Institute of Electrical and Electronics Engineers, Inc., New York, 1974. (Provided)

IEEE Std. 530-1978, "IEEE Standard Specification Format Guide and Test Procedure for Linear, Single-Axis, Digital, Torque-Balance Accelerometer," Institute of Electrical and Electronics Engineers, Inc., New York, 1978. (Provided)

IEEE Std. 529-1980, "Supplement for Strapdown Applications to IEEE Standard Specification Format Guide and Test Procedure for Single Degree-of-Freedom Rate-Integrating Gyros," IEEE Aerospace and Electronic Systems Society, Gyro and Accelerometer Panel, Institute of Electrical and Electronics Engineers, Inc., New York, 1980. (Provided)

IEEE Std. 813-1988, "IEEE Standard Specification Format Guide and Test Procedure for Two-Degree-of-Freedom Dynamically Tuned Gyros," IEEE Aerospace and Electronic Systems Society, Gyro and Accelerometer Panel, Institute of Electrical and Electronics Engineers, Inc., New York, 1989. (Provided)

IEEE Std. 647-1995, "IEEE Standard Specification Format Guide and Test Procedure for Single-Axis Laser Gyros," IEEE Aerospace and Electronic Systems Society, Gyro and Accelerometer Panel, Institute of Electrical and Electronics Engineers, Inc., New York, 1996. (Provided)

IEEE Std. 952-1997, "IEEE Standard Specification Format Guide and Test Procedure for Single-Axis Interferometric Fiber Optic Gyros," IEEE Aerospace and Electronic Systems Society, Gyro and Accelerometer Panel, Institute of Electrical and Electronics Engineers, Inc., New York, 1998. (Provided)

IEEE Std. 1293-1998, "IEEE Standard Specification Format Guide and Test Procedure for Linear, Single-Axis, Nongyroscopic Accelerometers," IEEE Aerospace and Electronic Systems Society, Gyro and Accelerometer Panel, Institute of Electrical and Electronics Engineers, Inc., New York, 1999. (Provided)

IEEE Std. 836-2001, "IEEE Recommended Practice for Precision Centrifuge Testing of Linear Accelerometers," IEEE Aerospace and Electronic Systems Society, Gyro and Accelerometer Panel, Institute of Electrical and Electronics Engineers, Inc., New York, 2001. (Provided)

IEEE Std. 1431-2004, "IEEE Standard Specification Format Guide and Test Procedure for Coriolis Vibratory Gyros," IEEE Aerospace and Electronic Systems Society, Gyro and Accelerometer Panel, Institute of Electrical and Electronics Engineers, Inc., New York, 2004. (Provided)

Junqueira, F., and de Barros, E., "Development of a Dynamically Tuned Gyroscope-DTG," ABCM Symposium Series in Mechatronics, Vol. 1, pp. 470-478, 2004. (Provided)

Kim, J., Lee, J-G, Jee, G-I, and Sung, T-K, "Compensation of Gyroscope Errors and GPS/DR Integration," 1996 IEEE Position Location and Navigation Symposium (PLANS), pp. 464-470, April 1996. (Provided)

Kim, H, Lee, J-G, Park, C., "Performance Improvement of GPS/INS Integrated System Using Allan Variance Analysis," presented at The International Symposium on GNSS/GPS, Sydney Australia, December 6-8, 2004. (Provided)

Lewis, C., and Kraft, M., "Simulation of a Micromachined Digital Accelerometer in SIMULINK and PSPICE," UKACC International Conference on Control, Vol. 1, Conference Publication No. 427, pp. 205-209, Sept. 1996. (Provided)

Maybeck, P. S., *Stochastic Models, Estimation, and Control*, Volume 1, Academic Press, New York, 1979.

Park, M., "Error Analysis and Stochastic Modeling of MEMS based Inertial Sensors for Land Vehicle Navigation Applications," UCGE Reports, Number 20194, University of Calgary, Department of Geomatics Engineering, April 2004.
[\(http://www.geomatics.ucalgary.ca/Papers/Thesis/YG/04.20194.MinhaPark.pdf\)](http://www.geomatics.ucalgary.ca/Papers/Thesis/YG/04.20194.MinhaPark.pdf)
(Provided)

Park, S., and Tan, C-W, "GPS-Aided Gyroscope-Free Inertial Navigation Systems," California PATH Research Report UCB-ITS-PRR-2002-22, California PATH Program, Institute of Transportation Studies, University of California, Berkeley, June 2002.
(Provided)

Rogers, R. M., *Applied Mathematics in Integrated Navigation Systems*, Second Edition, AIAA Education Series, American Institute of Aeronautics and Astronautics, Inc., Reston, VA, 2003.

Sharp, J., "Laser Gyroscopes," Lecture notes, Lasers & Electro-Optic Engineering 4, Department of Mechanical Engineering, University of Glasgow, Glasgow, Scotland, UK, 2000. (http://www.mech.gla.ac.uk/~sharpj/lectures/lasers/notes/laser_gyro.pdf)
(Provided)

Sutherland, R., and Overstreet, L., "Characterization of Non-Linear Error Terms for Vibrating Beam Accelerometers," Position, Location, and Navigation Symposium, 2006 IEEE ION, pp. 757-765, April 25-27, 2006. (Provided)

Thielman, L., Bennett, S., Barker, C., and Ash, M., "Proposed IEEE Coriolis vibratory Gyro Standard and Other Inertial Sensor Standards," 2002 IEEE Position Location and Navigation Symposium (PLANS), pp. 351-358, April 2002. (Provided)

11.0 SIMULINK Block Diagrams

The SIMULINK block diagrams listed below (by figure number) are provided on CD with this report. All block diagrams were generated using MATLAB (R2006a).

Figure 2. Translational Proof-Mass Accelerometer Open-Loop Block Diagram
(Dynamics-Only)

Figure 3. Translational Proof-Mass Accelerometer Closed-Loop Block Diagram
(Dynamics-Only)

Figure 4. Translational Proof-Mass Accelerometer Closed-Loop Block Diagram

Figure 5. Pendulous/Torque-Balance Accelerometer Open-Loop Block Diagram
(Dynamics-Only)

Figure 6. Pendulous/Torque-Balance Accelerometer Closed-Loop Block Diagram
(Dynamics-Only)

Figure 7. Pendulous/Torque-Balance Accelerometer Closed-Loop Block Diagram

Figure 9. Spring-Restrained Rate Gyro Open-Loop Block Diagram (Dynamics-Only)

Figure 10. Spring-Restrained Rate Gyro Closed-Loop Block Diagram (Dynamics-Only)

Figure 11. Spring-Restrained Rate Gyro Closed-Loop Block Diagram

Figure 12. Rate-Integrating Gyro Open-Loop Block Diagram (Dynamics-Only)

Figure 13. Rate-Integrating Gyro Closed-Loop Block Diagram (Dynamics-Only)

Figure 14. Rate-Integrating Gyro Closed-Loop Block Diagram

Figure 15. Ring Laser Gyro Open-Loop Block Diagram (No Errors)

Figure 17. Ring Laser Gyro Closed-Loop Block Diagram

Figure 18. Interferometric Fiber Optic Gyro Open-Loop Block Diagram (No Errors)

Figure 20. Interferometric Fiber Optic Gyro Closed-Loop Block Diagram

Figure 22. Coriolis Vibratory Gyro Closed-Loop Block Diagram

Figure 24. Dynamically Tuned Gyro Closed-Loop Block Diagram (Dynamics-Only)

Figure 25. Dynamically Tuned Gyro Closed-Loop Block Diagram